The fate of sub-micron circumplanetary dust grains II: Multipolar Fields

Daniel Jontof-Hutter[1] Douglas P. Hamilton[1]

Astronomy Department, University of Maryland, College Park, MD 20742-2421

ABSTRACT

We study the radial and vertical stability of dust grains launched with all charge-to-mass ratios at arbitrary distances from rotating planets with complex magnetic fields. We show that the aligned dipole magnetic field model analyzed by Jontof-Hutter and Hamilton (2012) is an excellent approximation in most cases, but that fundamentally new physics arises with the inclusion of non-axisymmetric magnetic field terms. In particular, large numbers of distant negatively-charged dust grains, stable in a magnetic dipole, can be driven to escape by a more complex field. We trace the origin of the instability to overlapping Lorentz resonances which are extremely powerful when the gravitational and electromagnetic forces on a dust grain are comparable. These resonances enable a dust grain to tap the spin energy of the planet to power its escape. We also explore the relatively minor influence of different launch speeds and the far more important effects of variable grain charge. Only the latter are capable of significantly affecting the micron-sized grains that dominate visible and infrared images of faint dust rings. Finally, we present full stability maps for Earth, Jupiter, Saturn, Uranus, and Neptune with magnetic fields modeled out to octupole order. Not surprisingly, dust in the tortured magnetic fields of Uranus and Neptune show the greatest instability.

1. Introduction

When Voyager 1 encountered Jupiter in 1979, the discovery of the tenuous dusty ring system came as a complete surprise. Although the earlier Pioneer missions found some hints of a ring system, many thought that dust close to Jupiter would rapidly spiral in by

gas drag (Owen *et al.* 1979). Voyager 2 confirmed the existence of the ring, and found the tiny satellites Metis and Adrastea that orbit inside the classical Roche limit and are the most likely source of ring material.

High speed impacts with small moons, as well as unseen large parent bodies, replenish the dusty rings with debris of all sizes. Similar sources of material for Saturn's tenuous inner D ring have not been found, though massive particles in narrow ringlets with enhanced local densities could serve as these sources (Showalter 1996; Hedman *et al.* 2007). In both environments, dust ejected by impacts from parent bodies have essentially collisionless trajectories. As debris particles acquire electric charges through interactions with the plasma environment and solar radiation, the smallest reach significant charge-to-mass ratios and, as a consequence, experience strong electromagnetic (EM) forces as they orbit through the magnetic field of their host planet.

For grains smaller than $\sim 1\mu$m in radius, the EM force exceeds perturbations from large satellites, the planetary oblateness and solar radiation pressure (Horányi *et al.* 1992). Even smaller dust grains may have orbits that are immediately unstable to either radial motion if the grains are positively-charged (Hamilton and Burns 1993a; Horányi *et al.* 1993a), or vertical motion (both positively- and negatively-charged: Northrop and Hill 1982). Many authors have studied various aspects of charged-particle dynamics. For a recent review, see Jontof-Hutter and Hamilton (2012), who derived analytic stability boundaries for the idealized case of grains with constant charge, launched at the Kepler speed in an aligned dipolar planetary magnetic field. As in that study, the boundaries between stable and unstable orbits are of particular interest to us here; these depend on the launch distance from the planet and the charge-to-mass ratio of an individual dust grain.

The aim of this paper is to explore the sensitivity of these stability boundaries to more realistic situations. We relax the idealized assumptions of Jontof-Hutter and Hamilton

(2012) above by considering i) non-zero ejecta speeds from the parent body, ii) higher-order magnetic field components, and iii) variable electric potentials on dust grains. We use Jupiter as our model planet since it has both a complex multipolar magnetic field and a well-studied dusty ring system (Burns *et al.* 1999; de Pater *et al.* 1999; Ockert-Bell *et al.* 1999; Brooks *et al.* 2004; Throop *et al.* 2004; Showalter *et al.* 2008; Krüger *et al.* 2009). After a detailed study of Jupiter, we then present stability maps for motion in the complex magnetic fields of Earth, Saturn, Uranus and Neptune. We begin by recapping stability results for a simple dipolar planetary magnetic field from Jontof-Hutter and Hamilton (2012).

2. Motion in an Aligned Dipolar Magnetic Field

The charge-to-mass ratio for Kepler-launched grains can be conveniently described by the ratio of the force induced by the corotational electric field of the planet with gravity, given by

$$L_* = \frac{q g_{10} R_p^3 \Omega_p}{G M_p m c} \tag{1}$$

(Hamilton 1993a,b; Jontof-Hutter and Hamilton 2012). Here, q and m are the electric charge and mass of a dust grain, g_{10} is the dipolar magnetic field strength at the equator, R_p and M_p are the planetary radius and mass respectively, Ω_p is the spin frequency of the planet, and G and c are the gravitational constant and speed of light. As a dimensionless independent variable, L_* accounts for all the relevant planetary parameters and avoids undue focus on the grain's size, shape, density and electric potential which are all poorly constrained. The sign of L_* depends on the product $q g_{10}$, and its value can easily be converted to a grain radius a_d for specified grain properties.

For large grains dominated by gravity and orbiting with semi-major axis a (the Kepler

limit), azimuthal, radial, and vertical motions have the same frequency

$$n_c = \left(\frac{GM_p}{a^3}\right)^{\frac{1}{2}}, \tag{2}$$

but for higher charge-to-mass ratios, these frequencies differ. As the charge-to-mass ratio is raised, these frequencies slowly diverge from one another (Hamilton 1993a), and for an aligned dipolar magnetic field, explicit expressions valid for all charge-to-mass ratios are available (Jontof-Hutter and Hamilton 2012). As these expressions will prove useful for our current study, we reproduce them here.

General motions in this problem can be conveniently separated into epicyclic motion about a guiding center which in turn circles the planet at an azimuthal angular speed ω_c. Where radial epicycles are small on the scale of the grain's orbit, balancing the centrifugal force, the EM force and gravity yields an expression for ω_c:

$$0 = \omega_c^2 + \frac{GM_pL_*}{r_c^3}\left(1 - \frac{\omega_c}{\Omega_p}\right) - \frac{GM_p}{r_c^3}. \tag{3}$$

(Northrop and Hill 1982; Mitchell *et al.* 2003; Jontof-Hutter and Hamilton 2012). Here and throughout, the subscript c refers to the guiding center of motion. The distance to the guiding center of motion, r_c, is just the semi-major axis a in the Kepler limit. Note that for gravity-dominated grains ($L_* \to 0$), we have $\omega_c^2 = GM_p/r_c^3 = n_c^2$ in agreement with Eq. 2. In the strong EM limit ($|L_*| \to \pm\infty$), $\omega_c \to \Omega_p$ and the grains are nearly locked to the magnetic field lines.

The radial or epicyclic frequency κ_c satisfies

$$\kappa_c^2 = \omega_c^2 - 4\omega_c\Omega_{gc} + \Omega_{gc}^2, \tag{4}$$

(Mendis *et al.* 1982; Mitchell *et al.* 2003; Jontof-Hutter and Hamilton 2012) at the guiding center, where $\Omega_{gc} = qB/mc = n_c^2 L_*/\Omega_p$ is the frequency of gyromotion. In the EM-dominated Lorentz regime, $\kappa_c = \Omega_{gc}$. In the gravity-dominated Kepler regime, $\Omega_{gc} \to 0$ and $\kappa_c \to n_c$, the Kepler orbital frequency, as expected.

Most grains are radially confined, suffering excursions of

$$r_g = \frac{r_L(\Omega_p - n_L)\Omega_{gL}}{\Omega_{gL}^2 - \Omega_{gL}(3\Omega_p + n_L) + n_L^2} \tag{5}$$

where r_g, the gyroradius, is much smaller than r_L, the launch distance. Here $n_L = \sqrt{GM_p/r_L^3}$ and $\Omega_{gL} = n_L^2 L_*/\Omega_p$ are the Kepler frequency and the gyrofrequency as determined at the launch distance (Schaffer and Burns 1994; Jontof-Hutter and Hamilton 2012). The epicyclic model fails only for positively-charged grains with $L_* \sim 1$, where the denominator in Eq. 5 becomes very small (see Jontof-Hutter and Hamilton 2012, Fig. 6b).

Finally, the vertical motion of grains with stable epicycles in the equatorial plane has frequency Ω_b, where

$$\Omega_b^2 = 3\omega_c^2 - 2n_c^2 + \frac{r_g^2}{\rho_c^2}\left(\frac{9}{2}\Omega_{gc}^2 - \frac{9}{2}\Omega_{gc}\dot{\phi}_c - \frac{3}{2}n_c^2\right) \tag{6}$$

(Jontof-Hutter and Hamilton 2012). Here, $\dot{\phi}_c = \omega_c - \Omega_p$ is the azimuthal motion of the guiding center in the frame rotating with the planet. Equation 6 is valid as long as $r_g/r_L << 1$ which holds in both the Kepler ($L_* \to 0$) and Lorentz ($L_* \to \pm\infty$) limits. In the Kepler limit, all three r_g^2 terms are negligible and $\Omega_b \to n_c$, while in the Lorentz limit, only the last two terms can be ignored and $\Omega_b^2 \to \frac{15}{2}\Omega_p^2 - 9\Omega_p n_c + \frac{5}{2}n_c^2$.

Where Ω_b tends to zero, grains in the equatorial plane become locally vertically unstable. Equation 6 provides good agreement with numerical data on the location and charge-to-mass ratio of boundaries between vertically stable and unstable grains, with two important caveats.

Firstly, in applying the epicyclic approximation, Eq. 6 assumes that radial motions are very small on the scale of the orbit ($r_g << r_L$). In addition, Eq. 6 is averaged over one gyrocycle, so the epicyclic motion must occur on a much shorter timescale than any stable vertical oscillations ($\kappa_c >> \Omega_b$). Both of these assumptions are easily met in the Lorentz

limit, but both lose accuracy as L_* decreases, particularly for the positively-charged grains which become radially unstable as $L_* \to 1$.

Secondly, setting $\Omega_b = 0$ determines local, as opposed to global, vertical stability in the equatorial plane of the spinning planet and its aligned dipolar magnetic field. Local instability is a necessary condition for global instability (whereby grains collide with the planet at high latitude), but it is not always sufficient. High-latitude restoring forces often lead to stable high latitude oscillations (HLOs) (Jontof-Hutter and Hamilton 2012). This class of orbits is more important for slow rotators like the Earth than it is at Jupiter or Saturn, but they do occur for the smallest grains inside $1.5R_p$ at Jupiter (Fig. 1).

With these two caveats in mind, we include the local and global stability boundaries found from numerical integrations by Jontof-Hutter and Hamilton (2012) for Jupiter with an aligned dipolar magnetic field model. Fig. 1 highlights these regions for a range of charge-to-mass ratios spanning four orders of magnitude and a suite of launch distances from Jupiter's surface to beyond its synchronous orbital distance, R_{syn}, with grains all launched at the local circular speed of the large parent bodies. Jontof-Hutter and Hamilton (2012) also derived analytic approximations to most of the boundaries in Fig. 1 (see their Fig. 9).

3.   Jupiter

We focus most of our attention on Jupiter as its magnetic field has been well studied, and is known out to octupole order (we adopt the O4 model of Acuna and Ness 1976; Dessler 1983). The planet's magnetic field is dominated by the dipolar terms: $g_{10} = 4.218$ Gauss, $g_{11} = -0.664$ Gauss, and $h_{11} = 0.264$ Gauss; these can be combined to determine the dipole tilt angle: $\arctan\left(\sqrt{(g_{11}^2 + h_{11}^2)}/g_{10}\right) = 9.6°$. The $g_{20} = $ -0.203 Gauss component can
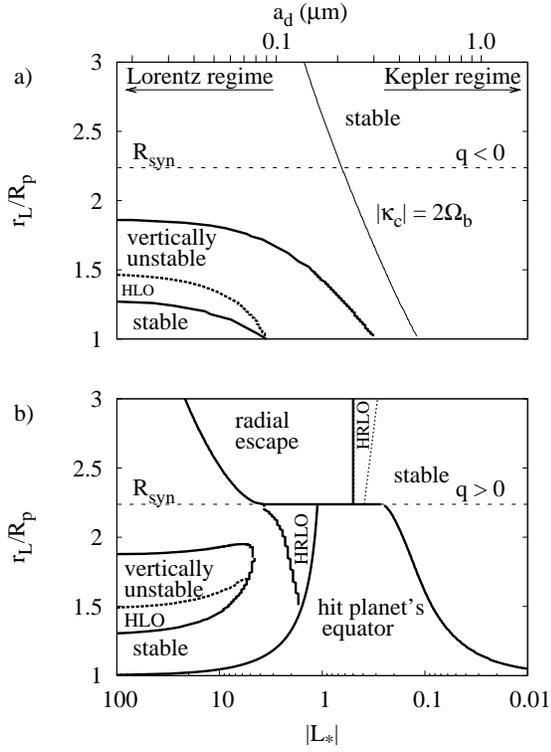
Fig. 1.— Stability boundaries for a) negative $(q < 0)$ and b) positive $(q > 0)$ grains in an aligned dipole magnetic field for Jupiter. This figure summarizes numerical data from Jontof-Hutter and Hamilton (2012), with grain radii marked along the top axis corresponding to a $-5V$ or $+5V$ potential on a spherical grain of material density 1 g cm^{-3}. The vertically-unstable grains depart from the equatorial plane and climb to high latitudes immediately after launch, ultimately colliding with the planet. Directly below this unstable region are grain trajectories with high latitude oscillations (HLOs). The radially unstable grains $(q > 0)$ escape if launched outside synchronous orbit (R_{syn}), or hit the planet if launched from within R_{syn}. Two regions of high radial and latitudinal oscillations (HRLOs) abut the radial instability region. Within R_{syn}, large inward radial excursions lead to vertical oscillations (roughly along magnetic field lines) which increase in amplitude until the grains strike the planet at high latitude. Outside R_{syn}, near $L_* = \frac{1}{2}$, some grains experience HRLOs indefinitely. Finally, for $q < 0$, a curve traces grains that experience HRLOs following the 2:1 resonance between the epicyclic (κ_c) and vertical (Ω_b) frequencies.

be interpreted as a southward vertical offset to the dipole field. Four additional quadrupolar and seven octupolar terms are known, and the upcoming Juno mission will measure still higher-order magnetic field coefficients for the first time. In this section, we add various effects to a simple aligned dipole model to elucidate their importance. We begin with non-zero launch speeds in the frame of the parent particle, as likely occurs with impact ejecta.

3.1. Varied Launch Speed

Typical ejecta velocities from an impact are tens to hundreds of meters per second in the rest frame of the parent body, in a cone centered on the impact velocity vector (de Pater and Lissauer 2010). Do these non-circular launch speeds significantly affect the stability of charged dust grains? To highlight the effect, we consider large initial velocities of 0.5 km s^{-1} in the prograde azimuthal (Fig. 2a) and radial (Fig. 2b) directions. Even with these large speeds, we note that EM-dominated grains on the left side of the plots are hardly affected. The Kepler speed at $r_L = 2.0R_p$ is $v_k =$29.8 km s^{-1}, while the local magnetic field lines rotate at $\Omega_p r_L=$ 25.1 km s^{-1}. The azimuthal impulse that we add, therefore, is only $\sim$10% of the $\Omega_{gc} r_g =$ 4.7 km s^{-1} gyrospeed and decreases the gyroradius r_g by a corresponding 10%. Although important, this effect is not noticeable on Fig. 2.

On the other hand, grains in the Kepler regime experience large radial excursions following a launch impulse. For an azimuthal boost ($\Delta v_\phi > 0$), we can solve for the semi-major axis a and eccentricity e from $r_L = a(1 - e)$, and

$$v_k^2 = GM_p \left(\frac{2}{r} - \frac{1}{a} \right). \tag{7}$$

For $\Delta v_\phi << v_k$, the radial motions extend outward from the launch position by $2ae \approx 4r_L \Delta v_\phi / v_k \approx 0.134R_p$ for the parameters of Fig. 2a. Although the intermediate-sized

– 10 –
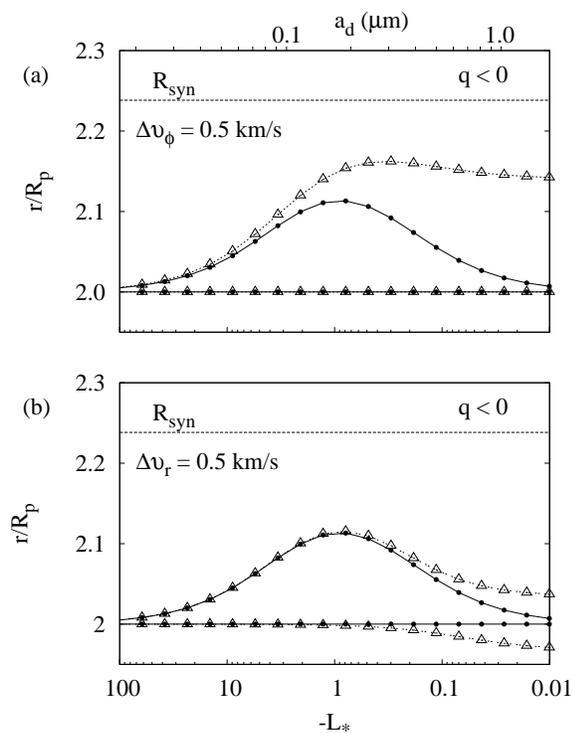
Fig. 2.— Radial range of motion for negatively-charged grains on initially circular orbits subject to a) an azimuthal (Δv_ϕ) and b) a radial (Δv_r) velocity impulse. The small filled circles indicate particles launched on circular orbits with $\Delta v = 0$, while the large open triangles denote those launched with $\Delta v = 0.5$ km s^{-1}. Synchronous orbit (R_{syn}) is indicated by a dashed line; the other lines simply track the data points.

grains have the largest radial excursions in Fig. 2a, the grains in the Kepler limit are most strongly affected by a Δv_ϕ kick.

Figure 2b shows that a radial impulse produces a more modest radial range of motion than an azimuthal boost. In this case, the impulse is perpendicular to the velocity of the parent body. For the smallest grains, in the Lorentz limit, this has almost no effect on the motion perpendicular to the field lines, and is akin to altering the initial phase but not the size of the gyrocycle. As with the azimuthal kick, a radial impulse has the largest effect for the largest grains. To first order in $\Delta v_r/v_k$, the orbital energy and semimajor axis are unchanged. The range of motion is therefore centered on the launch distance and has magnitude $2ae = 2r_L\Delta v_r/v_k \approx 0.067R_p$ for the parameters in Fig. 2b.

Figure 3 highlights the effect of velocity impulses on the stability boundaries of Fig. 1 for positively-charged grains in three orthogonal directions: a prograde azimuthal impulse ($\Delta v_\phi = +0.5$ km s^{-1}), a radial boost ($\Delta v_r = +0.5$ km s^{-1}), and a vertical kick ($\Delta v_z = +0.5$ km s^{-1}). In each case, the orbital stability boundaries are only moderately affected by these changes; circular orbits are thus often a good approximation when considering stability. Only the azimuthal impulse appreciably affects the orbital energy, and hence shifts the radial stability boundary (larger grains on the right in Fig. 3a). In this case, the positive Δv_ϕ increases the Kepler orbital energy significantly, thereby preventing grains near the right-most radial stability boundary from falling into Jupiter. A negative Δv_ϕ would destabilize grains near this boundary, permitting additional grains to fall to the planet. The left side boundary of the radially unstable zone is basically unaffected by all impulses, in agreement with Fig. 2.

The vertical stability boundaries are moderately affected by the Δv_ϕ (Fig. 3a) and Δv_z (Fig. 3c) initial impulses, but a radial impulse (Fig. 3b) has almost no discernable effect. Note that although in the Lorentz limit, the radial range of motion is too small to be
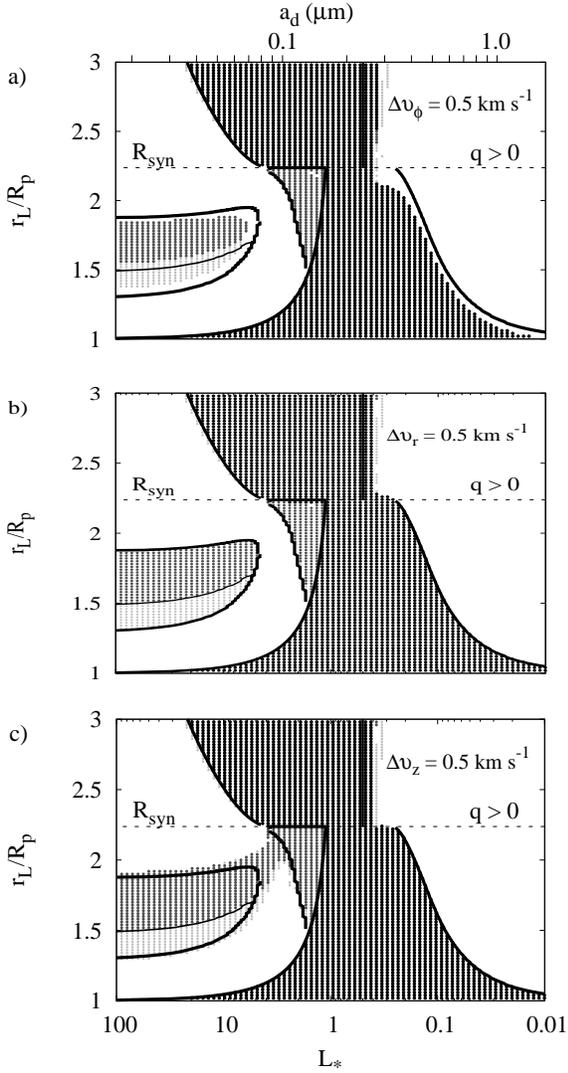
Fig. 3.— Stability of positive grains launched with a) an azimuthal launch speed $\Delta v_\phi = 0.5$ km s^{-1} faster than the local Kepler speed, b) $\Delta v_r = 0.5$ km s^{-1}, and c) $\Delta v_z = 0.5$ km s^{-1}, integrated over 0.1 years. The solid curves are the numerically-determined stability boundaries of Fig. 1 where grains are launched at the local circular Kepler speed. The darkest regions denote grains that collide with the planet near the equatorial plane or escape. Moderate grey marks grains that collide with the planet at high latitudes ($\lambda > \lambda_m = 5°$), while light grey shows HLO grains; locally unstable with vertical oscillations exceeding 5°, but bound globally. White regions mark locally-stable trajectories. Here, radial stability (central regions) is only significantly affected by Δv_ϕ while vertical stability (left-most regime) is affected by Δv_ϕ and Δv_z. A radial impulse, Δv_r, has no noticeable effects.

significantly altered with a Δv_ϕ launch impulse, the change in the area of a gyroloop, which alters the magnetic mirror force, still noticeably affects the high L_* stability boundary in Fig. 3a. Since $\Delta v_\phi > 0$ in Fig. 3a, the increased gyrospeed expands the gyroloop, leading to a stronger mirror force and hence a reduced region of vertical instability (Eq. 6). Enhanced instability results for $\Delta v_\phi < 0$. A vertical impulse Δv_z of either sign also leads to additional instability (Fig. 3c). For moderate values of L_* in particular, the Δv_z impulse causes the vertical instability region to dramatically expand near $L_* = 3, r_L = 2R_p$, and merge with the HRLO region of large radial and vertical oscillations (cf. Fig. 1). Negatively-charged grains (not shown) are similarly affected by 0.5 km s^{-1} impulses.

Overall, since the majority of real debris particles have much smaller speeds relative to their parent satellites than the 0.5 km s^{-1} considered here, we conclude that the stability boundaries are fairly insensitive to grain launch conditions. We note that new stability boundaries appropriate for non-circular initial orbits could be derived analytically using Hamiltonian methods (Northrop and Hill 1982; Schaffer and Burns 1994; Mitchell *et al.* 2003; Jontof-Hutter and Hamilton 2012), but as the effect is unimportant for our purposes, we turn instead to more complicated magnetic field geometries.

3.2. Vertically Offset Dipole

In this section we isolate the effect on orbital stability of Jupiter's dipole offset, modelled by the g_{10} and g_{20} magnetic field terms. The maps in Fig. 4 show that the offset field exacerbates the vertical instability for both negative and positive grains but has little effect on the radial stability boundaries. For the positive grains, the vertically unstable and HRLO zones overlap as in Fig. 3c.

In the equator plane, the g_{20} magnetic field is radial, and the corresponding $\vec{v} \times \vec{B}$ force
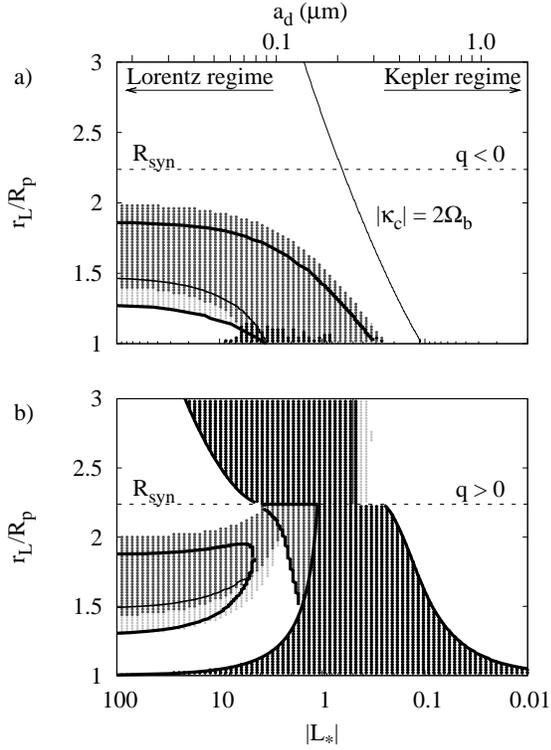
Fig. 4.— Stability of Kepler-launched negative grains (a) and positive grains (b) in a **vertically offset dipole field** for Jupiter, modelled with just the g_{10} and g_{20} magnetic field terms, and integrated for 0.1 years. The curves indicate the numerical stability boundaries for the centered and aligned dipole configurations from Fig. 1. In this map, the dark areas are radially unstable grains that either hit the planet or escape at low latitude ($|\lambda| < \lambda_m = 5°$). The moderately-grey regions are vertically unstable grains that collide with the planet at high latitude ($|\lambda| > \lambda_m$), and the light grey regions show HLO stable grains that exceed λ_m in latitude, the same criteria that we have adopted for the aligned dipole magnetic field of Fig. 3.

is vertical. Thus the g_{20} magnetic field term primarily adds an additional vertical force, thereby expanding the vertical instability. In fact, the stability map in Fig. 4b resembles Fig. 3c, which modelled a vertical impulse on the grains at launch; comparison of the two figures shows that the inclusion of g_{20} is a far more important effect. Note also that, unlike the effect of a Δv_z impulse, the offset dipole is effective at destabilizing grains near the planet, causing a significant vertical bounce oscillation and significantly expanding the region of global vertical instability.

3.3.   Tilted Dipole

In testing the effect of a tilted dipole field, we include the g_{10}, g_{11} and h_{11} magnetic field terms in our numerical models, setting g_{20} and all higher order terms to zero. Since the magnetic and gravitational equators do not coincide, we consider two separate equatorial launch phases: (i) $\phi_0 = 0°$, the ascending node of the magnetic equator on the geographic equator and (ii) $\phi_0 = 90°$, where the magnetic equator reaches its highest northern latitude of 9.6°. At this launch phase, many grains can reach latitudes $\approx 20°$ north and south of the equator, even if their trajectories are stable. Our stability results for negatively-charged grains are plotted in Fig. 5.

Although slight differences with launch phase are apparent, Figs. 5a and 5b are quite similar. Jupiter's tilt is a stronger effect than its offset (see Fig. 4a), extending the vertical instability boundary significantly outwards and close to R_{syn}. The dramatic outward expansion of the vertical instability can be understood as follows. For an aligned dipole, as synchronous orbit is approached, both the velocity relative to the magnetic field and the electromagnetic forces tend toward zero. Furthermore, as the velocity is azimuthal and the field is vertical, the direction of the weak EM force is entirely radial. For a tilted dipole, however, the magnetic field lines cross the equator plane with a radial component, causing
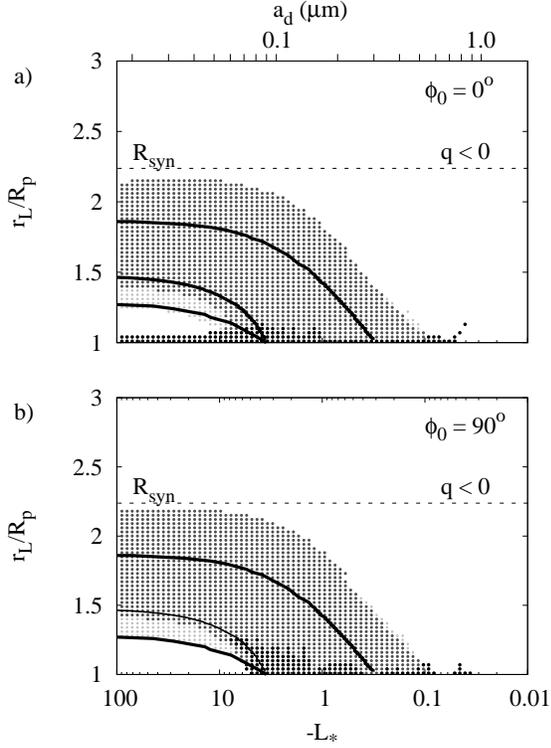
Fig. 5.— Stability of negative grains integrated over 0.1 years in a **tilted dipole field** for Jupiter, with the launch longitude at two locations; a) where the magnetic equator crosses the planetary equator plane ($\phi_0 = 0°$), and b) where the magnetic equator reaches its highest geographic latitude ($\phi_0 = 90°$). As before, the curves are the numerically-determined stability boundaries for the aligned dipole case from Fig. 1a. The grey scale is similar to Figs. 3 and 4: dark points are grains that collide with the planet at low latitudes, the moderately-grey region denotes grains that were vertically unstable to collide with the planet at latitudes higher than $\lambda_m = 20°$, the lightest grey marks trajectories that were excited to higher latitudes but remained bound, and the white areas represent grains that were locally stable. The only difference from Fig. 3 and 4 is that here we define low latitude to be $|\lambda_m| < 20°$ rather than $5°$.

a substantial $\vec{v} \times \vec{B}$ vertical force as with the offset dipole. These forces push particles out of the plane along field lines, leading to an expansion of the instability zone nearly to R_{syn}. Interestingly, the inner boundary at $(L_* = -50,\, r_L/R_p = 1.4)$ is far less affected.

One key difference in the two panels of Fig. 5 occurs for high L_* along $r_L/R_p = 1$; launching at the node $(\phi_0 = 0°)$ leads to collisions while launching at $\phi_0 = 90°$ does not. This difference is due to the curvature of the field lines in a dipole. In an aligned dipole magnetic field, stable mirror motion causes EM-dominated grains to oscillate about the magnetic equator, whereby the turning points or mirror points confine the latitudinal range of the grain. Launching from $\phi_0 = 90°$ in the tilted magnetic field ensures that the launch point is at one of the mirror points, and this vertical turning point is relatively close to Jupiter. Thus grains launched near $1R_p$ in Fig. 5b initially move radially outward and do not collide with the planet. By contrast, for grains launched at the node where $\phi_0 = 0°$, the mirror points are necessarily closer to the planet than the launch distance and, accordingly, we see that grains launched within $1.06R_p$ are forced to collide with Jupiter in Fig. 5a.

Another, more subtle difference between Figs. 5a and 5b, is that, grains launched at the node $(\phi_0 = 0°)$ are slightly more stable close to R_{syn} than those launched at $\phi_0 = 90°$ e.g. at $(L_* = -100,\, r_L/R_p = 2.21)$. In fact, both the inner and outer vertical stability boundaries are shifted slightly outwards for $\phi_0 = 90°$ compared to launches at $\phi_0 = 0°$.

Positively-charged dust grains are similarly affected by the addition of the dipole tilt. As with negative grains, we present two launch phases in Fig. 6, and find differences in orbital stability similar to those already discussed for Fig. 5. In particular, the azimuthal dependencies for highly-charged dust grains $(|L_*| \gg 1)$ are almost identical for both negative and positive charges (Fig. 6). As in Fig. 5a, grains launched immediately above the planet are unstable for $\phi_0 = 0°$ (Fig. 6a).

For all launch longitudes, the vertical instability expands greatly outwards, nearly

– 18 –
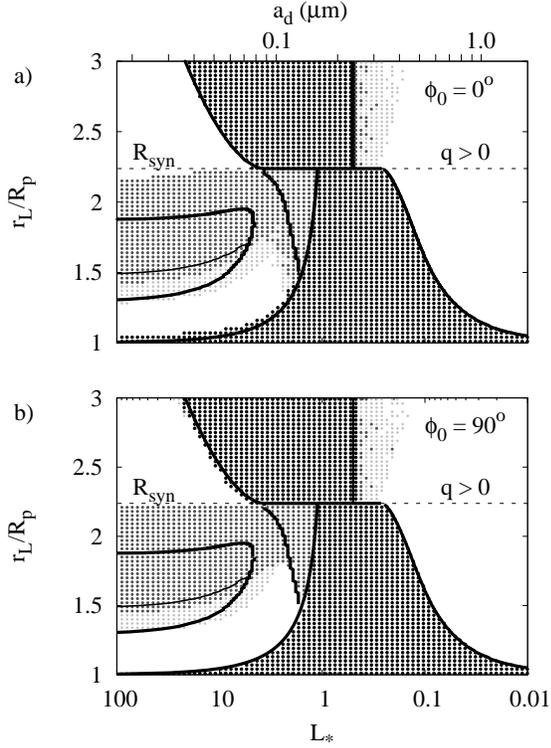
Fig. 6.— Stability of positive grains integrated for 0.1 years in a **tilted dipole field** for Jupiter, with two different launch longitudes: a) $\phi_0 = 0°$, where the magnetic equator crosses the planetary equator plane, and b) $\phi_0 = 90°$, where the magnetic equator reaches its highest geographic latitude. The solid black curves mark the stability boundaries for the aligned dipole case from Fig. 1b. As in Fig. 5, the darkest points denote grains that strike the planet at low latitude ($|\lambda_m| < 20°$, within twice the tilt angle), the moderate grey marks grains that strike the planet at high latitudes, the lightest grey marks grains that remain bound between high-latitude mirror points, and the white area represents grains that are vertically stable.

to synchronous orbit but very little towards the planet. As in Fig. 5, both the inner and outer vertical stability boundaries in the Lorentz limit are shifted slightly outwards for the $\phi_0 = 90°$ launches of Fig. 6b compared to the $\phi_0 = 0°$ launches of Fig. 6a. The two boundaries have slightly different explanations. For the outer boundary near R_{syn}, launching at $\phi_0 = 90°$ allows the initially larger vertical electromagnetic forces to drive the grain to higher latitudes where the gravity of the planet can overwhelm the centrifugal force and cause instability (Jontof-Hutter and Hamilton 2012). Near the inner vertical boundary, however, grains launched at the node $\phi_0 = 0°$ have a higher latitudinal range and are slightly less stable.

The radial stability boundaries are largely unaffected by the tilt in the magnetic field, although some slight differences are evident to the left of the radial instability region. Note the subtle difference along the left-most radial stability boundaries between Fig. 6a and Fig. 6b, where grains launched at $\phi_0 = 90°$ inside R_{syn}, are slightly more stable than those with $\phi_0 = 0°$. Outside synchronous orbit, however, the reverse holds true. This is most easily understood as an overall outward shift of the instability region from $\phi_0 = 90°$ to $\phi_0 = 0°$. Thus $\phi_0 = 90°$ grains behave almost exactly like $\phi_0 = 0°$ grains that have been launched a bit further from the planet. Note that this difference with launch phase was also seen for the negative grains with $r_L \approx R_p$ (Fig. 5), and the explanation is the same.

Until now we have only considered instabilities that remove a grain typically within a few hours. However, the tilted dipolar field causes further instabilities acting over weeks to months, and over a greater range of launch distances than the aligned dipolar case. We explore these longer-term effects below.

3.4. Resonant Effects in a Tilted Dipole Field

In an aligned dipole field, it can be shown that negative grains outside R_{syn} are permanently confined between their launch distance and R_{syn}; they are energetically unable to escape (Jontof-Hutter and Hamilton 2012). The tilted dipole field however, permits radial motion away from R_{syn}, and actually enables some negative grains to depart the planet, as was first seen by Hamilton (1996).

In Fig. 7, we show the stability maps for Jupiter modelled with the g_{10} and g_{11} magnetic field components for dust grains with both negative and positive charges whose trajectories were integrated for one Earth year. We seek to highlight the motion away from synchronous orbit for the negative grains, and towards R_{syn} for the positive grains, motions precluded by a simple aligned dipolar magnetic field.

Within synchronous orbit, the negatively-charged grains of Fig. 7a shows the same short-term instabilities seen in Fig. 5b. Notice in Fig. 7a, however, the large fingers of instability outside synchronous orbit. These features trace grains that suffer significant and unusual motions away from R_{syn}, and the largest one points towards $r_L/R_p = 3.55$ which happens to be the location of the outer 1:2 Lorentz resonance (Schaffer and Burns 1987, 1992; Hamilton 1994; Showalter *et al.* 2008). The other fingers point towards other Lorentz resonances. Importantly, the highly-detailed dark grey structures within these fingers (Fig. 7a) indicate significant numbers of negative grains that actually escape from Jupiter within one year.

These results are important for the escape of dust from the Io plasma torus, the most likely source of the jovian high-speed dust streams (Horányi *et al.* 1993b; Graps *et al.* 2000). Dust streams are comprised of radially-accelerated positively-charged dust grains, although in the plasma torus itself, dust-grain electric potentials are likely to be negative, even in sunlight (Bagenal 1994; Krüger *et al.* 2003). Lorentz resonances can provide a rapid
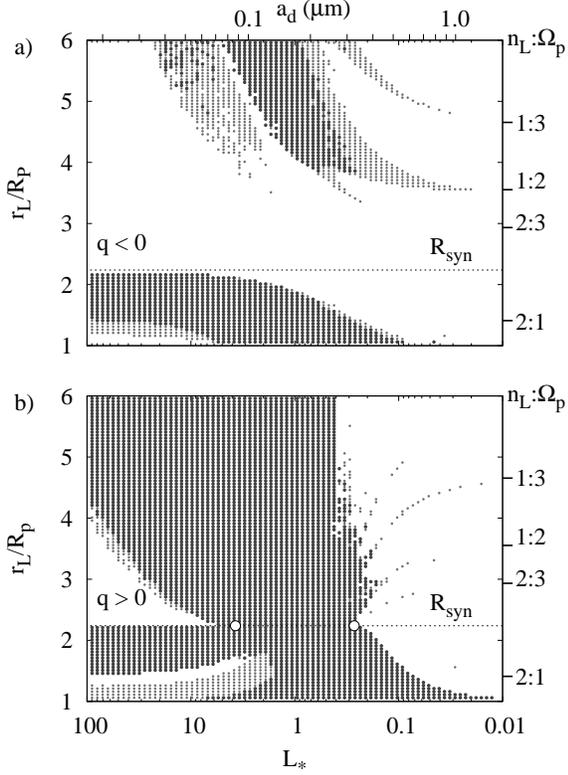
Fig. 7.— Destabilising effects of a **tilted dipole** magnetic field for Jupiter, with launch at $\phi_0 = 90°$. Integrations are for one Earth year, and we show a greater radial range than in Figs. 5 and 6. Note that the greyscale that we use here is also different from the earlier figures. Here, the darkest region denotes grains that either escape or crash into Jupiter within 1 year of launch. For the negative grains, the light grey marks grains with radial motions *away* from R_{syn} (in the direction opposite that expected for gyromotion), by at least $0.04 r_L$, revealing the destabilizing effect of the tilted magnetic field. For positive grains, the light grey indicates trajectories with radial motions towards R_{syn} of at least $0.02 r_L$. As always, white indicates stability.

escape mechanism for negatively-charged grains launched in the plasma torus. Once dust grains are free of the torus, charging currents become positive and the grains are accelerated outwards to escape. Our modelling in Fig. 7a actually understates the importance of this mechanism, as we force the potential to remain negative far outside the actual boundaries of the plasma torus.

For the positive grains, Fig. 7b shows an increased number of grains that are unstable, compared to Fig. 6b. The most striking difference is that in Fig. 7b, there are rough patches of additional radial instability just outside R_{syn} near ($L_* \approx 0.2$, $r_L/R_p = 3$). These unstable patches transition smoothly to become thin tracks of bound grains with excited radial ranges in the Kepler regime which, like the negative grains in Fig. 7a, point towards Lorentz resonances which occur for discrete integer ratios of the planetary spin and Kepler orbital frequencies.

Accordingly, we look to extend the concept of Lorentz resonances, (much studied in the Kepler limit by authors including Burns *et al.* 1985; Schaffer and Burns 1987, 1992; Hamilton and Burns 1993b; Hamilton 1994), to cover the entire range of charge-to-mass ratios. To determine the location of these Lorentz resonances in general, we start with the resonant equation

$$\dot{\Psi} = A\omega_c + B\Omega_p + C\dot{\Omega}_{node} + D\dot{\varpi}_{peri}, \tag{8}$$

where the coefficients A, B, C and D are integers that must sum to zero (Hamilton 1994). Here ω_c is the orbital frequency of the guiding center, Ω_p is the planetary spin rate, $\dot{\Omega}_{node}$ is the precession rate of the ascending node, $\dot{\varpi}_{peri}$ is the precession rate of the pericenter, and Ψ is the resonant argument; $\dot{\Psi}$ equals zero at a Lorentz resonance.

Equation 8 is completely general and valid for all charge-to-mass ratios if we are careful to rewrite $\dot{\varpi}_{peri}$ and $\dot{\Omega}_{node}$ in terms of our fully general frequencies from Eqs. 3 - 6. The

precession rates are simply differences between fundamental frequencies:

$$\dot{\varpi}_{peri} = \omega_c - |\kappa_c| \tag{9}$$

and

$$\dot{\Omega}_{node} = \omega_c - \Omega_b \tag{10}$$

where κ_c, the epicyclic frequency of motion, is negative by convention for retrograde epicycles. Recall that in the gravity limit, $\omega_c = |\kappa_c| = \Omega_b = n_c$ and hence $\dot{\varpi}_{peri} = \dot{\Omega}_{node} = 0$, as expected. As an illustration, we focus on radial resonances for which $C = 0$.

Setting Eq. 8 to zero and using Eq. 9 to eliminate $\dot{\varpi}_{peri}$, we find:

$$- B\omega_c + B\Omega_p - D|\kappa_c| = 0 \tag{11}$$

or

$$B\dot{\phi}_c + D|\kappa_c| = 0, \tag{12}$$

since in the frame corotating with the magnetic field, the azimuthal frequency of the guiding center is given by $\dot{\phi}_c = \omega_c - \Omega_p$.

Equation 12 shows that a Lorentz resonance affecting radial oscillations reduces to a simple ratio between the epicyclic frequency $|\kappa_c|$, and the motion of the guiding center relative to the rotating magnetic field ($\dot{\phi}_c$). Our approach thus shows how to extend classical Lorentz resonances to remain valid at arbitrary charge-to-mass ratios.

In Table 1, we show select Lorentz resonances for all charge-to-mass ratios and their driving magnetic field terms, taken from Hamilton (1994). In the Kepler limit, these Lorentz resonances act to slowly increase eccentricities and/or inclinations, destabilizing trajectories over many orbits. The resonances that include multiple instances of $\dot{\varpi}_{peri}$ or $\dot{\Omega}_{node}$, such as the three 1:3 and 1:4 resonances in Table 1, are weaker since their strengths in the Kepler regime depend on higher powers of the small quantities e (eccentricity) and

$\vec{B}$-field terms	Res. name	r_L $(L_* \to 0)$	Res. frequency $\dot\Psi$	Corotating form
g_{11}	1:4	5.64 R_p	$4\omega_c - \Omega_p - 2\dot{\varpi}_{peri} - \dot\Omega_{node}$	$\dot\phi_c + 2|\kappa_c| + \Omega_b$
g_{11}	1:3	4.66 R_p	$3\omega_c - \Omega_p - \dot{\varpi}_{peri} - \dot\Omega_{node}$	$\dot\phi_c + |\kappa_c| + \Omega_b$
g_{11}	1:2	3.55 R_p	$2\omega_c - \Omega_p - \dot\Omega_{node}$	$\dot\phi_c + \Omega_b$
g_{21}	1:3	4.66 R_p	$3\omega_c - \Omega_p - 2\dot{\varpi}_{peri}$	$\dot\phi_c + 2|\kappa_c|$
g_{21}	1:3	4.66 R_p	$3\omega_c - \Omega_p - 2\dot\Omega_{node}$	$\dot\phi_c + 2\Omega_b$
g_{21}	1:2	3.55 R_p	$2\omega_c - \Omega_p - \dot{\varpi}_{peri}$	$\dot\phi_c + |\kappa_c|$
g_{22}	2:4	3.55 R_p	$4\omega_c - 2\Omega_p - \dot{\varpi}_{peri} - \dot\Omega_{node}$	$2\dot\phi_c + |\kappa_c| + \Omega_b$
g_{22}	2:3	2.93 R_p	$3\omega_c - 2\Omega_p - \dot\Omega_{node}$	$2\dot\phi_c + \Omega_b$
g_{22}	2:1	1.41 R_p	$\omega_c - 2\Omega_p + \dot\Omega_{node}$	$2\dot\phi_c - \Omega_b$

Table 1: Selected Lorentz resonances (column 2), driven by the magnetic field coefficient in column 1, appear, for small charge-to-mass ratios, at the locations given in column 3. The resonance frequency is given in its most general form (column 5) and in a second form most useful when gravity dominates (column 4).

i (inclination). At higher charge-to-mass ratios, however, all of these resonances increase in strength, and their effects on grain orbits occur on much shorter timescales than in the Kepler regime. Some negative grains at $6.0R_p$ in Fig. 7 escape in as little as a few days.

Figure 8 overlays the strictly radial Lorentz resonances of Table 1 on the stability map for a tilted dipolar field (the data from Fig. 7a). For negative grains outside synchronous orbit, the Lorentz resonances curve upwards directly into the region of escape for increasing L_*. This occurs because the epicyclic frequency $|\kappa_c|$ increases rapidly with L_* (Eq. 4); $\dot{\phi}_c$ must also increase to maintain a given resonance (Eq. 12). Since $\dot{\phi}_c$ increases away from R_{syn}, remaining in resonance as $|\kappa_c|$ increases necessitates a greater launch distance from synchronous orbit. Although these curves are determined from frequencies that are strictly valid only for an aligned dipole field, they nevertheless show an impressive match to our data, despite the more complex magnetic field.

For the positive grains, the resonant tracks in Fig. 8b begin at the same locations in the Kepler limit as for negative grains, but they curve towards synchronous orbit as L_* increases. On the right side of the short-term radial instability of Fig. 1, all resonant solutions converge to a single point at $(L_* = 2 - \sqrt{3},\ r_L = R_{syn})$. This is the point at synchronous orbit where $|\kappa_c| = \dot{\phi}_c = 0$, and grain orbits are locally unstable in even a simple aligned dipolar field (Jontof-Hutter and Hamilton 2012). The convergence to synchronous orbit as L_* increases occurs because for positive grains with $L_* << 1$, $|\kappa_c|$ decreases as L_* increases (Eq. 4), and so $\dot{\phi}_c$ must decrease as well (Eq. 12), driving distances towards R_{syn}.

The Lorentz resonances destabilize the motion of grains, and hint that a non-axisymetric field allows the negative grains to tap into planetary rotation, to make escape energetically favorable. The detailed structure in the stability map of Fig. 8, including the escaping negatively-charged grains, is due only to the effects of g_{10} and g_{11}. The first-order theory, however, can only explain the three 1:N resonances (Table 1) and not the instability of the
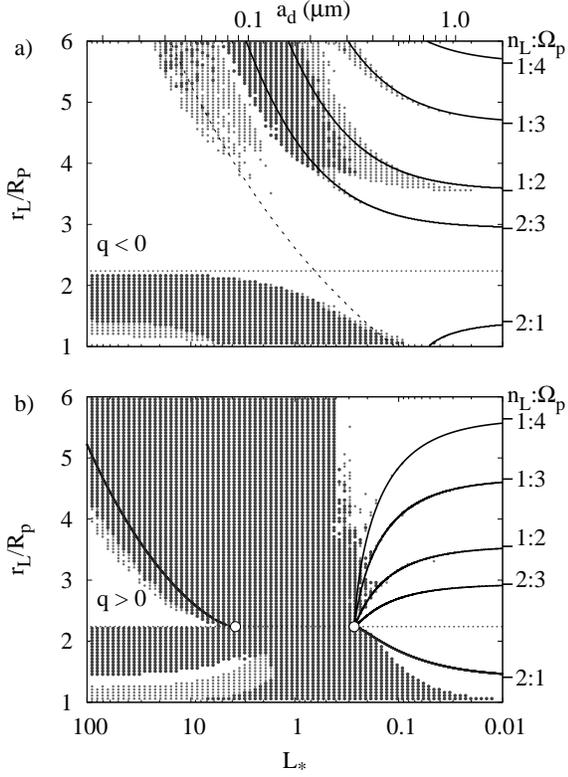
Fig. 8.— The **tilted dipole** stability map of Fig. 7 with theoretical curves $\dot{\Psi} = 0$ for radial resonances only from Table 1 superimposed as solid curves. The theoretical curves fall atop the instability "fingers" seen in Fig. 7a, and the trails of points from Fig. 7b, attesting to the accuracy of the theory. The 2:1 resonance between epicyclic frequency $|\kappa_c|$ and vertical Ω_b motions is also shown in the upper panel, as a dashed curve. In the lower panel, the open circles mark the points ($L_* = 2 \pm \sqrt{3}$, $r_L/R_{syn} = 1$), where $\dot{\phi}_c = \kappa_c = 0$ and all resonant tracks for positive grains converge. For large L_*, all radial resonances lie nearly atop one another in panel b).

2:3 and 2:1 resonances, which nevertheless are definitely present in Figs. 7 and 8. We will return to explain this discrepancy shortly.

In addition to Lorentz resonances of the type shown in Eq. 8, there are also resonances between the dust grain's radial and vertical motions, analogous to the Kozai resonance experienced by highly-inclined orbits. The dominant resonance of this type satisfies: $\omega_c - 2\dot{\Omega}_{node} + \dot{\varpi}_{peri} = 0$, such that $|\kappa_c| = 2\Omega_b$. This 2:1 resonance between radial and bounce motions is the strongest of its type since during one bounce period, north-south symmetry ensures that the dust grain experiences two cycles in magnetic field strength (Jontof-Hutter and Hamilton 2012). The resonance track also passes close to the high charge-to-mass boundary of the resonant structure in Fig. 8a. We turn now to investigate the effects of the individual asymmetric quadrupolar magnetic field terms which should also power resonances (Table 1).

3.5. Quadrupole Terms

In this and the following sections, we focus on the escaping negative grains outside synchronous orbit, because these escapes are the most fundamental new effect added by a non-axisymmetric magnetic field. In the stability maps of Fig 9, we isolate the effects of g_{21} and g_{22} to highlight their respective Lorentz resonances, as compared to the stability boundaries of the tilted dipole from Fig. 7a (solid curves). For stable negatively-charged grains in an aligned dipole field, radial motion is always confined between the launch distance and synchronous orbit. Thus, as in Fig. 7a, the light grey data in Fig. 9 trace where grain trajectories show motions away from R_{syn} that are significant on the scale of the launch distance.

The g_{21} and g_{22} terms studied in Figs. 9a and 9b clearly cause less overall instability
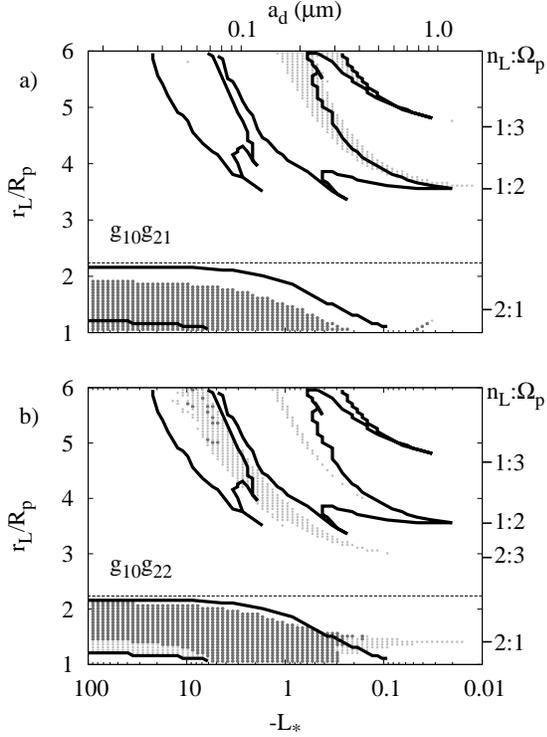
Fig. 9.— **Quadrupole-order terms** isolated in stability maps for negatively-charged dust: To g_{10} we add just g_{21} in panel a) and just g_{22} in panel b), with a 1-year simulation for each dust grain. The light grey marks stable grains whose radial excursions *away* from R_{syn} exceeded 4% of the launch distance, while dark grey indicates collision just as in Fig. 7a and 8a. The dark curves mark the envelope of instability when just the g_{10} and g_{11} coefficients are included, from the numerical data of Fig. 7a.

than g_{11} in Fig. 7a. Consider first, motion within synchronous orbit. The g_{21} term (Fig. 9a) is nearly as effective as g_{11} in inducing vertical instability, and in fact is better able to clear out the region just above the planet's cloudtops. The effect of the g_{22} term (Fig. 9b) is similar to, but typically weaker than, g_{11} with one important exception. Note the long, horizontal feature extending towards the 2:1 inner Lorentz resonance in the Kepler regime (small L_*). These stable grains are strongly stirred by the 2:1 vertical Lorentz resonance excited by g_{22} (Table 1). A similar effect can be seen on the right-hand side of Fig. 9a; a small trail of points near $(r_L/R_p \approx 1.05, L_* \approx -0.03)$ hints that g_{21} causes a weak 2:1 inner Lorentz resonance. However, the first-order theory of Hamilton (1994) predicts that g_{32} rather than g_{21} should excite this resonance!

Outside R_{syn}, the situation is more straightforward. Figure 9a shows that the g_{21} term strongly excites the 1:3 and 1:2 Lorentz resonances, as expected from Table 1. Notice that the 1:2 resonance is significantly stronger than the 1:3 resonance because, in the Kepler limit, the former has a strength proportional to the small orbital inclination i while the latter's strength depends on the product of two small quantities e and i, where e is the orbital eccentricity (Hamilton 1994). Interestingly, in one way the g_{21} term has a stronger effect on radial motion than the g_{11} term, extending the 1:2 and 1:3 resonances further into the Kepler limit. This can be understood from Table 1 and Hamilton (1994), which show that the g_{21} term should naturally excite both of these resonances.

Figure 9b shows two main features from the g_{22} term outside R_{syn}, which tend towards 1:2 and 2:3 in the Kepler limit. The g_{22} term excites vertical motions (Hamilton 1994), which are not traced directly in Fig. 9, but which clearly couple to radial motions. This causes the outer 1:2 and 2:3 resonances seen in Fig. 9b, as well the strong inner 2:1 resonance that reaches far into the Kepler regime. A glance at Table 1 shows that g_{22} excites a first-order 2:3 inclination resonance and a second-order mixed and therefore weaker

2:4 resonance, accounting for the differing responses of grains near these resonances visible in Fig. 9b.

We are left with a few paradoxes. First, how does the g_{11} magnetic field term excite the 2:3 and 2:1 Lorentz resonance? And how does the g_{21} term excite the inner 2:1 resonance? To answer these questions, we require a second-order expansion of the Gaussian perturbation equations (Danby 1988), for the electromagnetic force. The first-order Fourier series expansion in the small parameter L_* was obtained by Hamilton (1994) for each magnetic field coefficient by treating the orbital elements as constants. To extend this to second order, we take the Fourier series first-order solution for each orbital element and insert it on the right-hand side of the Gaussian perturbation equations. Simplifying requires identities for the product of two trigonometric functions and we end up with second-order L_*^2 corrections to the time rates of change of the orbital elements. Thus the power in each resonant frequency in Table II of Hamilton (1994) is augmented by a second-order correction. Calculating the strength of these corrections is a straight-forward but unenlightening exercise which we do not undertake here, as the calculation is clearly invalid for $L_* > 1$ when the third- and higher-order terms cannot be ignored. Indeed, the very concept of orbital elements also breaks down for $L_* > 1$ when electromagnetism is no longer a small perturbation to gravity.

Instead, we explore the form of the corrections and show how magnetic field coefficients can excite resonant terms other than those shown in our Table 1 and in Table II of Hamilton (1994). Consider first the $g_{10}g_{11}$ simulation of Figs. 7 and 8. To second order in L_*, this combination of coefficients excites two relevant 2:3 resonances: $\dot{\Psi} = 3\omega_c - 2\Omega_p - \dot{\varpi}_{peri}$ and $\dot{\Psi} = 3\omega_c - 2\Omega_p + \dot{\varpi}_{peri} - 2\dot{\Omega}_{node}$, both with amplitude proportional to $L_*^2(R_p/r)^6 g_{11}^2 ei^2$. In addition, a 2:1 resonance, $\dot{\Psi} = \omega_c - 2\Omega_p + \dot{\varpi}_{peri}$ is also excited, with amplitude also proportional to $L_*^2(R_p/r)^6 g_{11}^2 ei^2$. These resonances show up in Figs. 7 and 8 near the planet

where (R_p/r) is relatively large, near instability boundaries where e and/or i are large, and for particles where L_* itself is relatively large. Comparison of the data in Fig. 7b with the corresponding curves in Fig. 8b shows that these resonances are weaker than the already-discussed first-order resonances, as expected.

In a similar manner, the second-order theory shows that g_{21} also drives the 2:1 resonance with frequency $\dot{\Psi} = \omega_c - 2\Omega_p + \dot{\varpi}_{peri}$ and amplitude $L_*^2 g_{21}^2 (R_p/r)^8 e^3$ (Fig. 9a). The rest of Figs. 9a and 9b appear to be well explained by the linear theory of Hamilton (1994), which predicts both pairs of instability outside R_{syn}.

The second-order corrections, however, should excite the resonant frequency $\dot{\Psi} = 5\omega_c - 4\Omega_p + \dot{\varpi}_{peri} - 2\dot{\Omega}_{node}$ with amplitude proportional to $L_*^2 (R_p/r)^8 g_{22}^2 ei^2$; the tiny weak feature just below the 2:3 track and near the center of Fig. 9b may be due to this resonance. Furthermore, the frequency $\dot{\Psi} = 3\omega_c - 2\Omega_p - \dot{\varpi}_{peri}$ with amplitude proportional to $L_*^2 (R_p/r)^8 g_{21}^2 e^3$, should excite particle motions in Fig. 9a, but no evidence for these motions is seen. This may be due to the fact that horizontal resonances driven by g_{21} are intrinsically weaker than the vertical resonances driven by g_{22} (Hamilton 1994). In any case, given the strong drop in the strength of second-order corrections with distance, their effects outside R_{syn} are minimal.

3.6. Realistic Full Magnetic Field Models

Figure 10a combines the effects of all dipolar and quadrupole terms for negative grains. Within synchronous orbit, all grains in the Lorentz limit are now unstable, as are all grains within the g_{11} envelope. Furthermore, g_{22} powers a 2:1 vertical resonance with frequency $\dot{\Psi} = \omega_c - 2\Omega_p + \dot{\Omega}_{node}$, seen as the dominant horizontal feature extending from the instability region (inside R_{syn} in Fig. 10a). Adding the octupole term g_{32} strengthens this feature by

exciting a 2:1 radial resonance $\dot{\Psi} = \omega_c - 2\Omega_p + \dot{\varpi}_{peri}$ (Fig. 10b). These resonances have the most dramatic effect on large dust grains near the planet, due to rapid decline in magnetic field strength with distance for higher-order terms. The g_{33} octupole term adds a spike of instability at the 3:2 resonance as well ($\dot{\Psi} = 2\omega_c - 3\Omega_p + \dot{\Omega}_{node}$).

Outside R_{syn}, a large region of escaping negative grains exceeds the sum of the effects of g_{11} (Fig. 7a), g_{21} (Fig. 9a) and g_{22} (Fig. 9b), although the main resonant tracks are easily identified. In particular, a huge swath of grains centered on $L_* = 5$ at $r_L/R_p = 5$ escapes here, but is bound for the simpler field geometries of Figs. 7a, 9a, and 9b.

Adding the octupole magnetic field coefficients (Fig. 10b) presents only subtle differences from the quadrupole model of Fig. 10a outside R_{syn}. In particular, the locations of the resonant tracks appear to be unchanged. The three narrow fingers in the center of Fig. 10b, however, are noticeably more prominent than the corresponding structures in Fig. 10a. The outer 2:3 resonance is driven by the g_{22} term ($\dot{\Psi} = 3\omega_c - 2\Omega_p - \dot{\Omega}_{node}$), but the 3:4 and 4:5 resonances cannot be excited by quadrupole terms in the linear theory. The 3:4 resonance is driven by the g_{33} coefficient, but also by a second-order term proportional to $g_{11}g_{22}$. Both are active in the lower plot, while only the latter affects the upper plot. Similarly, the 4:5 resonance is excited by the non-linear g_{22}^2 term (both plots) and by the $g_{11}g_{33}$ term (bottom plot only). As always, when multiple resonances are active, chaos ensues and escape becomes more likely. Note that these differences between Figs. 10a and 10b are confined within $\sim 4R_p$, due to the rapid radial weakening of the high-order magnetic field terms.

In general, we see numerically and analytically that Lorentz resonances widen in strength as L_* increases. This causes the resonances to overlap and destabilize most of the grains near $L_* = -1$ if grains are launched beyond the immediate vicinity of synchronous orbit. As $|L_*|$ increases, higher-order dependencies on the charge-to-mass ratio permit even
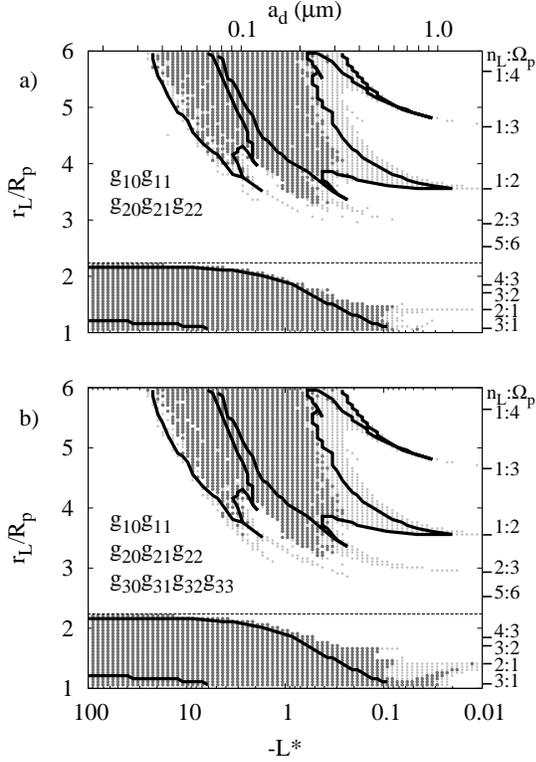
Fig. 10.— Resonant **quadrupolar and octupolar effects** in stability maps for negative dust grains: To the tilted dipole model of Fig. 7a, shown here as the solid curves, we add all quadrupole terms (panel a), and all terms out to octupole order (panel b). The darkest regions mark grains that collide with the planet or escape during a 1-year integration. The lighter grey indicates stable grains whose radial excursions *away* from R_{syn} exceeded 4% of the launch distance, as in Figs. 7a, 8a and 9.

more resonances to emerge and vie for control of dust grain dynamics.

In Fig. 11, the vertical and radial Lorentz resonances for negative and positive grains are atop the stability map for Jupiter's full magnetic field modeled out to octupole order. For the negative grains of Fig. 11a, as L_* increases going from right to left, all the radial resonances diverge rapidly from R_{syn}. Most of the vertical resonances however, diverge from synchronous orbit more slowly as $|L_*|$ increases, and in the Lorentz regime these pile up on the vertical stability boundary inside R_{syn} (Fig. 1a), where $\Omega_b \to 0$ and hence, by the resonant condition, $\dot{\phi}_c \to 0$. The combined effects of many vertical resonances near this boundary destabilizes all grains in the Lorentz regime out to synchronous orbit in Fig. 11a.

For the positive grains of Fig. 11b, all radial resonances converge on the two locally unstable points along R_{syn}. In the Lorentz regime, the curve outside synchronous orbit satisfies $\kappa_c \to 0$. This is further to the left of the stability boundary for an aligned dipole (Fig. 1b), ensuring that resonances pile up and further destabilize grains with the additional magnetic field terms in the Lorentz regime. Physically, it means that smaller grains are more likely to be expelled for a particular positive electric potential than calculated using the aligned dipolar approximation. For the larger grains, in the Kepler regime, the vertical Lorentz resonances asymptote near the $L_* = 1/2$ boundary where the guiding center distance rapidly increases and the bounce frequency $\Omega_b \to 0$.

For both positive and negative grains where $|L_*| << 1$, the outer 1:3 radial and vertical resonances coincide implying $\dot{\varpi}_{peri} = \dot{\Omega}_{node}$. This is indeed the case to first order in L_* as was first deduced by Hamilton (1993a). The result can also be obtained from our Eqs. 3, 4 and 6.

In the Kepler regime, N:N+1 resonances pile up at synchronous orbit (like the 5:6 resonance marked in Fig. 11a); for higher N, these are driven by g_{NN} and g_{NN-1} magnetic field terms beyond the octupole model that we have considered here. Thus our numerical
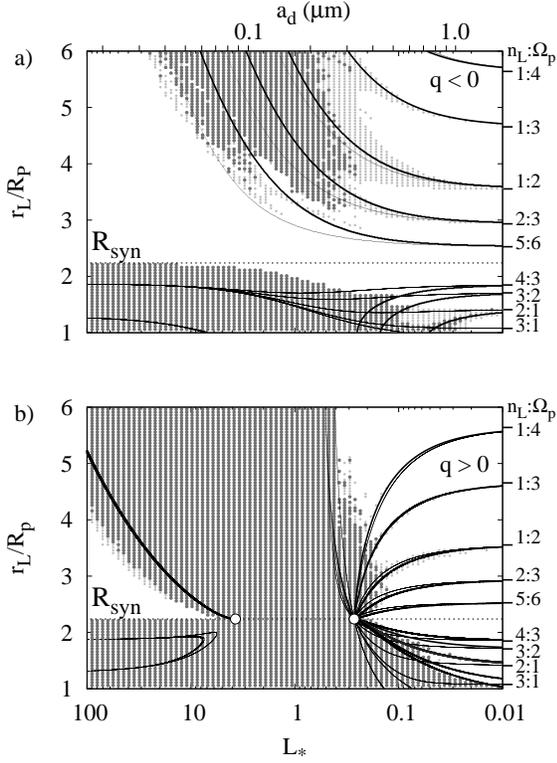
Fig. 11.— Theoretical resonance curves over all charge-to-mass ratios superimposed on a stability map of Jupiter's full magnetic field for a) negative grains (from Fig. 10b) and b) positive grains. The dark grey marks dust grains that escaped or crashed into Jupiter during the 1-year integration. The faint grey points denote grains that experience radial motions away from synchronous that exceeded 4% of the launch distance for the negative grains, and towards R_{syn} by at least 2% of r_L for the positive grains. The thick bold curves mark radial Lorentz resonances, and the thin curves track the vertical Lorentz resonances. At synchronous orbit $\dot{\phi}_c = 0$, and the white circles mark the local stability threshold from Jontof-Hutter and Hamilton (2012) where $\kappa_c \to 0$.

model of Jupiter's magnetic field is incomplete and the inclusion of higher-order terms would lead to some additional escapes. Given the strong radial dependence of higher-order magnetic field components, we expect changes to be limited to regions close to the planet and at high L_*, just like the differences between Figs. 10a and 10b. Nevertheless, we eagerly await the improved magnetic field model that the Juno spacecraft will soon provide. In the meantime, we now relax our assumption of a constant grain-charge.

4. Variable grain charge in an aligned dipolar field

The electric charging of a circumplanetary dust grain is a function of the plasma environment, the flux of solar radiation, and the physical properties of the grain itself. Since the nature of the grains and their plasma environment are poorly constrained, the motion of any particular grain with a varying charge is highly model dependent. Our goal in this section is not to pick the best model for a given situation, but rather to elucidate the physics of orbital changes driven by charge variations. Possibly the simplest non-trivial model which nevertheless, must occur in circumplanetary applications is the shutoff of the photoelectric current during planetary shadow passages (Horányi and Burns 1991). This effect will be present even if all other model-dependent charging effects are absent. The azimuthal asymmetries that the shadow induces has a profound effect on dust grain motions, as we shall soon see.

Returning to our aligned dipolar magnetic field model, and assuming that the plasma distribution is perfectly axisymmetric, the effect of the planetary shadow transit is to introduce a strong azimuthal asymmetry in the charging environment for a dust grain. In the shadow, the photoelectric effect of sunlight is absent, and interactions with the plasma cause a net negative charge on the grains (Schaffer and Burns 1987). In the sunlight, by contrast, equilibrium typically favors a slight positive electric potential. Fig. 12 highlights
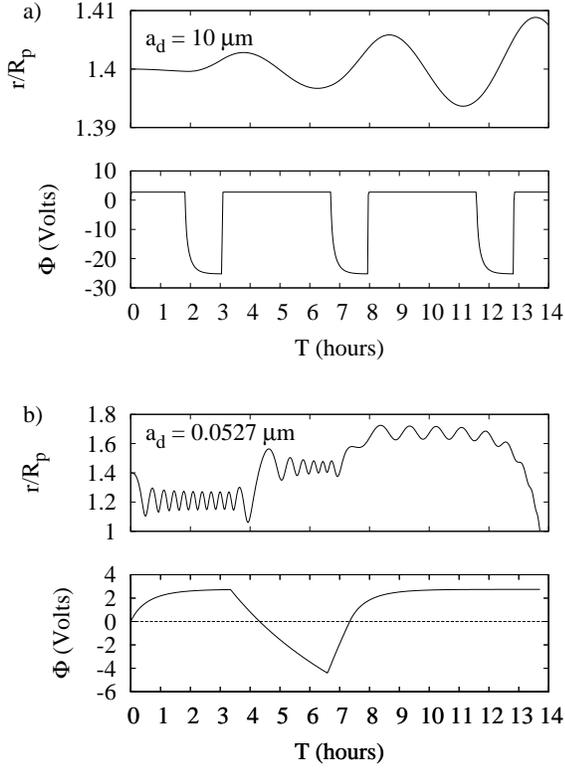
Fig. 12.— The charge response of a dust grain in plasma and sunlight depends on grain size. Here we show a) 10 μm and b) 0.0527 μm grains, launched at 1.4 R_p at local noon, with an aligned dipole magnetic field for Jupiter, in a uniform plasma with density $n_e = 1.4$ cm^{-3} and temperature $T_e = 10$ eV. The grains initially carry no charge. Each panel shows the grain's radial trajectory and instantaneous electric potential Φ in Volts. The large grain experiences three 1-hour long shadow passages during which the charge decreases, while the smaller grain has a single 3-hour eclipse, and much more sluggish changes to its electric potential.

the differing effect of charge variation with grain size, given identical launch distances. Here, we have chosen two example grains launched inside synchronous orbit at a location that avoids the short term vertical instability of Fig. 1.

Firstly, we note that the equilibrium charge on a sunlit dust grain is 2.75 Volts, whereas in the shadow, the equilibrium electric potential is -27 Volts. The large grains reach their equilibrium potential far more rapidly than the smaller grains. Indeed, the charge response is typically inversely proportional to the size of the dust grain (Horányi and Juhász 2010). For the larger grain in Fig. 12a, the increasing amplitude of the radial oscillations is caused by the fact that charge variation repeats each dust grain orbit, thereby resonating with the epicyclic frequency for grains in the Kepler regime. This is the destabilizing shadow resonance (Horányi and Burns 1991; Hamilton and Krüger 2008) which we will find strongly affects our stability map.

In Fig. 12b, the smaller dust grain does not have enough time to reach charge equilibrium during its three-hour shadow passage. This dust grain experiences stochastic kicks both radially inwards and outwards from its launch distance; the grain eventually becomes vertically unstable and crashes into the planet at high latitude after just 14 hours. Each kick in the guiding center distance r_c occurs when the electric potential on the dust grain is ~1 Volt, when the instantaneous value L_* places the grain near the left-most radial stability boundary of Fig. 1b. When the potential is higher than 2 Volts or negative, the grain experiences stable radial oscillations. The decreasing amplitude of these oscillations with time is due to the grain reaching higher charge-to-mass ratios ($|L_*|$), and hence experiencing tighter gyrations. After several random steps in r_c due to the grain's periodic encounters with the radial instability, it moves into the vertical instability zone (Fig. 1) and is lost to Jupiter.

In Fig. 13 we present stability maps for a large range of grains sizes from 0.001μm

to 10μm, over a broad range of launch distances, to test the effect of charge variations on orbital stability. In these models, dust grains are free to vary their charge as the environment allows, both with the effects of the shadow present (Fig. 13b), and explicitly ignored (Fig. 13a).

Without the planetary shadow, grain charges quickly converge to equilibrium values, and the stability map in Fig. 13a looks very similar to one for a constant (positive) charge (Fig. 1b). In Fig. 13a, the superimposed bold-faced curves, corresponding to a +2.75 Volt constant potential, match the data very closely on far right. Since the electric potentials of the large grains rapidly converge to equilibrium, the Kepler-regime side of the radial instability also closely conforms to the analytical boundaries of Jontof-Hutter and Hamilton (2012). The smaller grains, however, take significant amounts of time to reach charge equilibrium. The grains just to the left of the left-most solid curves in Fig. 13a either escape (outside R_{syn}) or fall into the planet (inside R_{syn}), before they have enough time to reach their equilibrium charge. While these tiny grains experience modest electric charges, a different set of stability curves to the left of those in Fig. 13a applies. Within 1.2 R_p, for example, 0.01 μm sized grains collide with Jupiter within a few hours while the characteristic charging time is a day. Similarly, outside synchronous orbit, 0.01 μm-sized grains just outside the radially unstable zone for constant +2.75 Volt grains can still escape the planet. These grains, initially neutral, charge up slowly in the sunlight. Hence, even if their equilibrium charge would permit stable motion, the time spent in the radially unstable regime causes them to collide with Jupiter or escape before reaching charge equilibrium.

With the planetary shadow turned on, the shadow resonance acts to increase eccentricities, destabilizing grains over a far broader range of sizes than than those that remain at their equilibrium potential. For the largest of these grains ($a_d \gtrsim 1\mu m$), the shadow transit destabilizes grains over timescales commensurate with the precession due
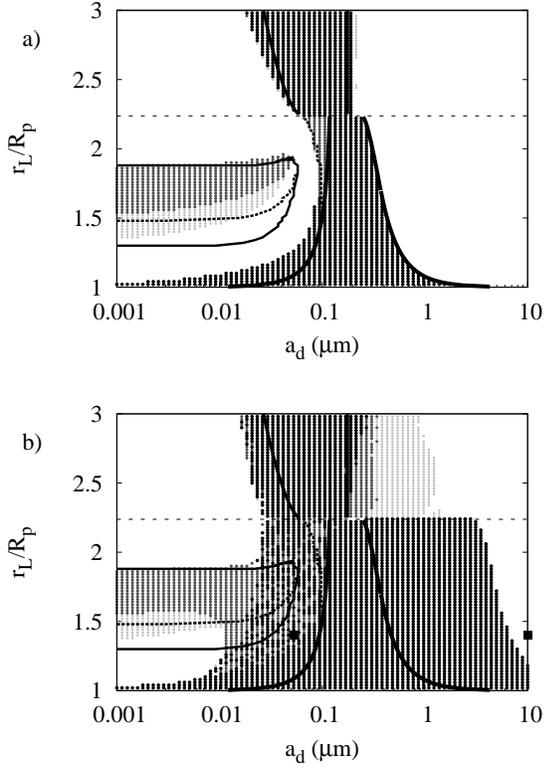
Fig. 13.— Stability of grains with variable charge response to plasma for two grain charging models: a) constant photoelectron emission, and b) a more realistic photoelectric response which is interrupted during shadow transit. We adopt an aligned dipole for Jupiter's magnetic field, and neglect its 3.12° obliquity. Grains, all launched at local noon, begin with zero electric potential and are integrated over 1 year, a timescale long enough to cover the orbital precession in the Kepler regime due to J_2, which is included in our model of the gravity field. Consistent with the greyscale in Figs. 3 and 4, the darkest region denotes radial instability-either collision with the planet or escape within $\lambda_m = 5°$ of the equator plane- the moderate grey represents high-latitude collisions with Jupiter, and the lightest grey marks surviving grains with high latitude oscillations. The two filled squares correspond to the trajectories illustrated in Fig. 12. Note that the horizontal axis, now marking increasing grain radius as L_* is no longer constant, spans twice the range as in previous figures. In both a) and b), the numerical boundaries are included for an assumed electric potential of +2.75 Volts.

to the gravitational J_2 term (Horányi and Burns 1991). Thus we include the J_2 term in our model for Fig. 13, and adjust launch speeds to ensure launch from a circular orbit. The smallest grains in Fig. 13b respond to changes in the charging environment over a longer timescale. Thus, grains that survive the initial charging process (the stable grains of Fig. 13a) reach an electric potential that deviates little from its mean over the orbital period, and hence the shadow has little effect on grains smaller than 0.01μm in size. This region of Fig. 13b essentially matches Fig. 1b in the Lorentz limit, with either vertical instability or stable high-latitude oscillations between 1.29 R_p and 1.70 R_p.

Grains between 0.01μm and 0.1μm launched outside 1.2 R_p, but within R_{syn}, experience charge variations that cause them to spend some fraction of each orbit in a radially unstable regime. Eventually they strike the planet, although the timing for this is unpredictable. As we saw in Fig. 12b, such grains experience random walks in radial location but do not cross synchronous orbit. Roughly half the grains in this region of Fig. 13b collided with the planet at high latitudes.

Grains larger than 0.5μm launched outside R_{syn} in Fig. 13b experience excited radial motions and vertical motion close to the radial stability boundary of Fig. 13a ($L_* = \frac{1}{2}$, Hamilton 1993a; Jontof-Hutter and Hamilton 2012), which extends the Thebe ring away from Jupiter (Hamilton and Krüger 2008). Inside R_{syn}, Fig. 13b shows that the shadow resonance destabilizes grains more than 10 times bigger than the largest grains destabilized with the shadow switched off. The boundary between stable and unstable here is determined not by the time of the integration but by the precession timescale due to the higher-order J_2 gravity field component at Jupiter (≈ 0.25 years in the main ring, and longer further out).

We emphasize that resonant charge variation on dust grains due to the photoelectric current clearly has an important effect on grain dynamics. Epicyclic motion also provokes resonant charge variations due to both radial gradients in the plasma properties and the

– 42 –

varying dust-plasma speed with gyrophase. Of the effects studied so far: launch speeds, realistic magnetic fields and time-variable electric charges, the latter appears to be the most important. Non-zero launch impulses, by contrast, are a minor effect on grain-orbit stability. The relative importance of the different effects, however, will vary dramatically with plasma properties.

For example, in a dense plasma like the Io plasma torus, the equilibrium charge is always negative (as in Figs. 7a and 8a) even in full sunlight. Spatial or temporal gradients in plasma properties can also have a profound effect. Since all of the parameters for charging are very uncertain, we leave a thorough study of these effects for another paper. The constant charge maps here and in Jontof-Hutter and Hamilton (2012) are still relevant though, serving as a measure of the minimum instability in a given system. It is also a good approximation for planets with significant obliquities, where dusty rings spend much of their host's long orbital period in direct and uninterrupted sunlight.

Accordingly we turn to the other major magnetospheres of the Solar System and construct stability maps for dust grains with constant charge in complex multipolar magnetic fields.

5.   Other planets

After our detailed investigation of Jupiter, we are now in a position to map and interpret stability results for each of the magnetized planets in the Solar System. We begin with the planet with the simplest magnetic field, Saturn.

5.1. Saturn

Saturn's full magnetic field can be described by an aligned dipole with a slight vertical offset (Cao *et al.* 2011). We model the full field with $g_{10} = 0.2154$, $g_{20} = 0.0164$ and $g_{30} = 0.0274$ Gauss (Connerney *et al.* 1984). Figure 14a shows the stability map for negatively-charged grains, with the numerically-determined stability boundaries for an aligned and centered dipole included for comparison, as in Fig. 4.

As at Jupiter, (see Fig. 4) Saturn's dipole offset increases the instability of grains to vertical perturbations. This eliminates the stable zone close to the planet that we see for the aligned dipole case, and moves the outer vertical stability boundary significantly further from the planet. The effect is stronger at Saturn than at Jupiter due to its relative large g_{20} term and to the larger R_p/R_{syn} at Saturn, making the planet a bigger target. By contrast, at Jupiter (see Fig. 4), a large locally-stable region in the Lorentz limit close to the surface and at high $|L_*|$ survives the inclusion of g_{20}.

For positively-charged grains, in Fig. 14b, the offset dipolar field causes the vertical instability to join the radial instability, as in Fig. 4b. However, a tiny island of globally stable grains survives near $(L_* = 3, r_L/R_p = 1.3)$. The radial stability boundaries for an aligned dipole field for Saturn (Jontof-Hutter and Hamilton 2012), match Saturn's full magnetic field remarkably well.

At Saturn we also see a slightly wider range of charge-to-mass ratios excited by the 2:1 resonance between epicyclic and vertical motions, when compared to Jupiter (Fig. 4a). This is due to the range of launch distances extending further out in units of R_{syn} in Fig. 14a. The accuracy of the theoretical curve matching this resonance vindicates the use of an aligned dipole approximation for Saturn's magnetic field to calculate radial and vertical orbital frequencies.
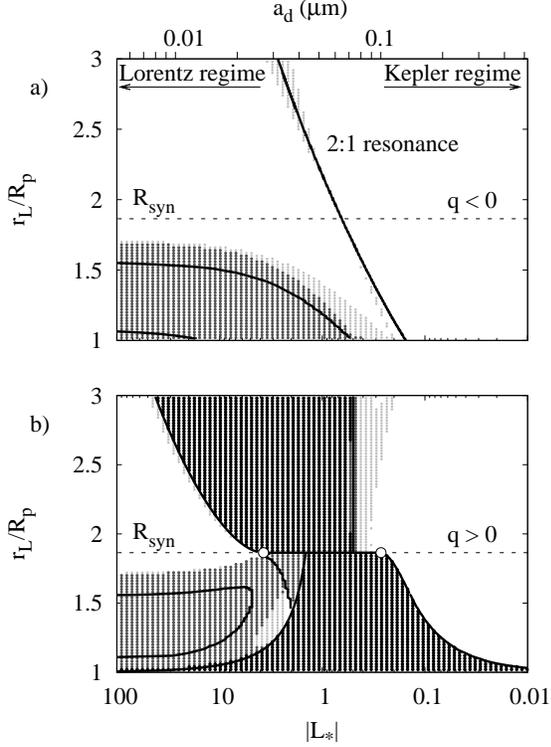
Fig. 14.— Stability of a) negative and b) positive Kepler-launched grains, followed for 0.1 years in Saturn's full magnetic field. The greyscale matches that of Figs. 3 and 4. The darkest region denotes grains that are radially unstable to escape or strike the planet (positive charges only), the moderate grey scale marks trajectories that were vertically unstable to climb out of the ring plane and strike the planet at high latitude, the light grey scale marks grains that are vertically unstable in the equatorial plane but remain globally bound with mirror points further than $|\lambda_m| = 5°$ from the equator, and the white area marks locally stable orbits. Superimposed on the data are the numerically-determined stability boundaries for an aligned and centered dipolar magnetic field model for Saturn (Jontof-Hutter and Hamilton 2012), as well as the curve marking the analytical 2:1 resonance between epicyclic and vertical motion, which closely tracks band of grains that reach high latitudes but remain bound. The white circles mark the local stability threshold at R_{syn}, where $L_* = 2 \pm \sqrt{3}$.

The transition from grains that are lost to the vertical instability to those that remain bound in the B ring is at $1.70R_p$ or $\approx 102,000$ km in the Lorentz limit (Fig. 14). This is close to a large increase in optical depth in the B ring that begins around $1.72R_p$, and losses to erosion may play a role in ring evolution across this boundary. Northrop and Connerney (1987) argued for a link between the inner edge of B ring and the vertical stability boundary. Their model for vertical motion predicted all highly-charged grains to be unstable within $1.54R_p$ at Saturn, close to the sharp inner edge of the B ring. Their model, however, did not provide a detailed mechanism and also invoked poorly understood electrostatic effects (Northrop and Hill 1983; Northrop and Connerney 1987). Voyager 2 data revealed another transition in optical depth between 1.63 R_p and 1.65 R_p (98,000 - 99,000 km), a few thousand kilometers inside the vertical stability boundary at Saturn with its full magnetic field configuration. While the proximity of this transition to the vertical stability boundary is intriguing, a detailed model to explain this congruency remains elusive.

5.2. Earth

The Earth's magnetic field is dominated by a dipole tilted by a moderate 11.4° from the axis of rotation. For our full-field models, we use magnetic field coefficients out to octupole order from Roberts and Soward (1972). For the Earth, $g_{10} < 0$ and the magnetic field is inverted compared to all of the giant planets. Thus for the Earth, $L_* > 0$ for negatively-charged grains, and it is these negative grains that suffer the radial instability (Jontof-Hutter and Hamilton 2012).

Figure 15 compares the stability of grains in Earth's full magnetic field to an aligned dipolar model. With an aligned dipolar field, the vertical instability at Earth in the Lorentz limit is local, leading to a region of high-latitude globally-stable oscillations. For the positive grains ($L_* < 0$, Fig. 15b) this locally vertically unstable region curves towards the

planet as $|L_*|$ decreases, and only a small range of grains launched near the surface between $L_* \approx -0.1$ and -1.0 collides with the planet. This changes very little with the inclusion of Earth's higher-order magnetic field terms, as Fig. 15 indicates. More dramatically, the higher-order terms (primarily g_{11}) expand the vertical instability in the Lorentz limit to further distances, almost to R_{syn}. In this region, grains do in fact collide with the planet. The feature is very similar to what we saw at Jupiter in Figs. 5 and 6, except that the global instability region is far narrower in the case of the Earth. Just as at Jupiter, tilting the magnetic field does not significantly move the inner vertical stability boundary of Fig. 15b. For the negative grains, Fig. 15a shows that the vertical instability is also displaced towards R_{syn} and curves slightly upwards to merge with the region of radial instability. The expansion of the vertical instability for both positive and negative charges nearly to synchronous orbit has a unique benefit in assisting the removal of dusty space debris from this crowded region of Earth orbit (Horányi *et al.* 1988; Juhász and Horányi 1997; Valk and Lemaître 2008).

The radial instability in Fig. 15a, however, looks very different at Earth than at Jupiter (compare Figs. 6 and 15a). Nevertheless, outside synchronous orbit, the higher-order magnetic field terms have little effect and the radial stability boundaries of Jontof-Hutter and Hamilton (2012) match the data remarkably well. Inside synchronous orbit, the more complicated magnetic field slightly extends the area of HRLOs that abut the disjoint regions of equatorially-confined radial instability. Thus Earth's full magnetic field barely alters the radial instabilities expected for an aligned dipole: The few unstable grains that exceed the radial stability boundary on the right side of Fig. 15a may be associated with Lorentz resonances. In particular, the small cluster of points near ($L_* = 0.01$, $r_L/R_p = 2.0$) closely corresponds to the inner 6:1 Lorentz resonance. All else being equal, the Lorentz resonances are more important close to the planet where the magnetic field irregularities are strongest.
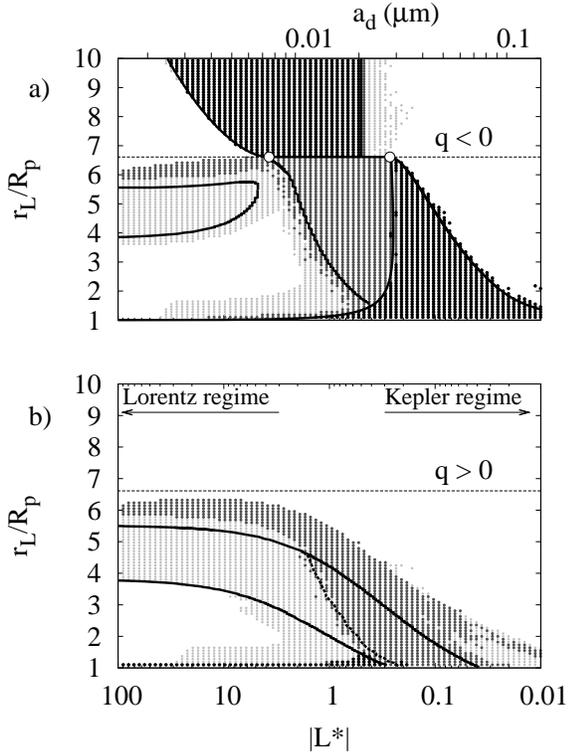
Fig. 15.— Stability of Kepler launched negative (a) and positive (b) grains in Earth's magnetic field complete to octupole order, integrated over 1 year, with launch at $\phi_0 = 0$. The solid curves mark the numerical stability boundaries for the Earth with its anti-aligned g_{10} component alone (Fig. 12 from Jontof-Hutter and Hamilton 2012). Grains in the darkest region, (negative charges only) crashed into the planet or escaped at a latitude less than twice Earth's 11.4° tilt angle. The moderate grey region marks grains that struck the planet at latitudes higher than twice the tilt angle, the light grey marks grains with stable vertical oscillations with mirror points exceeding twice the tilt angle in latitude, and white regions are the remaining stable orbits. The white circles mark the points $L_* = 2\pm\sqrt{3}$, at $r_L = R_{syn}$, where grains are on the threshold of radial instability.

As an exercise, we compared the results displayed in Fig. 15 with a simpler tilted dipole model, including just the g_{10} and g_{11} terms (figure not shown). The main difference that arises is that the positive and negative grains that are excited to high latitudes, near ($|L_*| = 10$, $r_L/R_p = 1.3$) are not excited in the tilted dipole model. A more subtle difference is the extra set of collisions to the right of the radial instability boundary on the right-hand side of Fig. 15a marking grains that were lost because of Lorentz resonances. These grains survive in the simple tilted dipole model. Deviations at greater distances are not expected due to the steep radial dependence of the quadrupole and octupole terms, and indeed, they are not seen. All in all, a tilted magnetic dipole is a robust model for the motion of charged dust grains at the Earth.

5.3. Uranus

Uranus' complex magnetic field destabilizes grains for a much wider range of charge-to-mass ratios than Jupiter, Saturn or Earth. Figure 16 shows the stability of grains launched at Uranus, with magnetic field coefficients out to octupole order taken from Ness *et al.* (1991). This figure highlights the significant dependence of launch azimuth on grain lifetimes. We determined grain orbit stability for 12 equally-spaced azimuthal launch positions, and followed trajectories for 1 year.

Beyond R_{syn}, the full Uranian magnetic field causes a large class of grains to escape rapidly, for both negatively- and positively-charged dust. In general the stability maps for negative and positive grains are very similar, especially inside synchronous orbit. Within R_{syn}, all trajectories in the Lorentz limit appear unstable for both negative and positive charges, which significantly constrains the low-energy plasma environment in the uranian ring system. Furthermore, both Figs. 16a and 16b show far more dependence on launch phase at high charge-to-mass ratio, on the left side of the stability maps, than on the right,

consistent with our results for Jupiter (Fig. 6).

Uranus' magnetic tilt as well as its quadrupole and octupole magnetic field coefficients are much more important when compared to its g_{10} term than at Jupiter or Saturn, causing strong Lorentz resonances, and hence a dramatic expansion of escaping negative grains over that seen at Jupiter in Fig. 10b. Furthermore, at Uranus, grains as close as R_{syn} can escape, unlike at Jupiter. In Fig. 16a, a spike at $(L_* = -0.03, r_L/R_p = 2)$ appears to be associated with the 2:1 inner Lorentz resonance that approaches the Kepler limit at 2.04 R_p. Interestingly, this resonance appears stronger for negative grains than for positive ones. At Jupiter, two spikes in Fig. 10b distinguish the inner 2:1 vertical and radial resonances. Similarly, at Uranus, Fig. 16a hints at an even stronger pairing of destabilizing 2:1 resonances, one curving downward towards the planet as $|L_*|$ increases, and one arcing slightly upward.

5.4. Neptune

We model Neptune's magnetic field configuration with data from Connerney *et al.* (1991). As for Uranus, above, the stability map includes the effect of launch longitude on grain-orbit stability. And as with Fig. 16, Fig. 17 indicates the number of 12 equally-spaced launch azimuths that survive a 1-year integration.

Figure 17a maps the stability of negatively-charged dust at Neptune, and includes a large region of escaping negative grains, though this range of is slightly smaller at Neptune than at Uranus (Fig. 16a). However, the escape region for negative grains is still much more significant at Neptune than at Jupiter (see Fig. 10b), and it too reaches R_{syn}. As at Uranus, grain orbit stability on the Lorentz-dominated side of Figs. 17a and 17b is strongly dependent on the launch phase. Inside synchronous orbit, grains in much of the
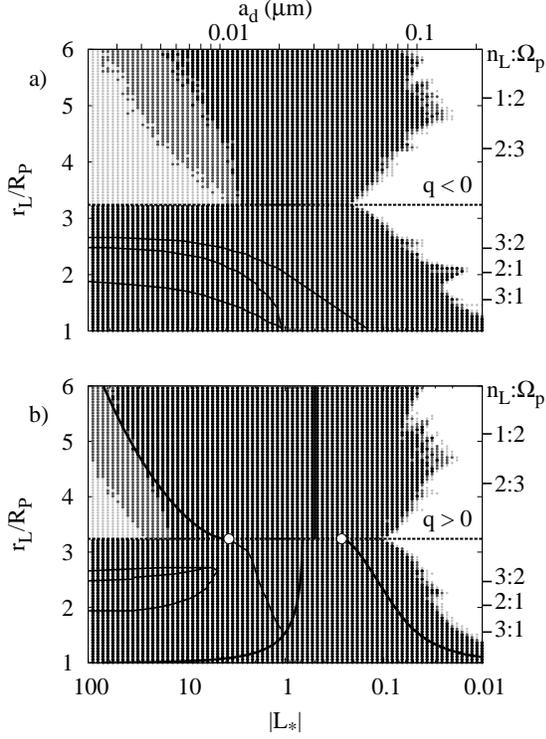
Fig. 16.— Stability of Kepler-launched grains in Uranus' full field over one year. There are three shades of grey, plus white to highlight the effect of azimuthal launch position on grain orbit stability. The darkest grey marks grains that were unstable for all of 12 equally-spaced launch longitudes. The intermediate grey denotes unstable trajectories for 6 to 11 launch positions, the lighter grey 1 to 5 launches, and the white regions were stable for all launch positions. The embedded curves mark the Uranian equivalent of those in Fig. 1, the stability boundaries for an aligned dipole magnetic field model. The white circles mark the local radial stability at R_{syn}, where $L_* = 2 \pm \sqrt{3}$.

highly-charged Lorentz limit are unstable, except for a small region around $r_L/R_p = 2.2$ for both positive and negative grains, where stability varies significantly with launch phase. This contrasts with Uranus, where all grains inside R_{syn} in the Lorentz regime were unstable. Again, however, the instability at Neptune vastly exceeds that of Jupiter.

In the Kepler-dominated regime of Fig. 17a, two spikes most likely associated with the inner 2:1 Lorentz resonance feature prominently. Just as we saw at Uranus, in Fig. 17b, this inner 2:1 resonance appears to be weaker. For negative grains, the white stable zone to the right in Fig. 17a reaches to higher L_* values (smaller grain radii) than we saw for Uranus (Fig. 16a). For both planets, the dependence on azimuthal launch position for stability is only important for $|L_*| >> 1$. In the Kepler regime, grains move rapidly across magnetic field lines, and instabilities are effectively averaged over all launch phases. All evidence points to greater instability at Uranus than at Neptune. This is consistent with the Uranian dipole tilt of 59° exceeding Neptune's 47°.

6. Discussion

In this paper, we have studied three main effects on charged particle motion: i) non-zero launch velocities from orbiting parent bodies ii) complex magnetic fields and iii) time-variable electric charges. We presented data from over 250,000 numerical integrations and compared our results to analytical theories, extending the important concept of Lorentz Resonances to arbitrary charge-to-mass ratios, and showed that effects of order L_*^2 can explain results that the linear theory of Hamilton (1994) misses.

Non-zero launch impulses (section 3.1), relative to the Kepler flow have little effect on charged-grain dynamics and stability. Radial stability boundaries are only noticeably affected by an azimuthal kick. Vertical instability, by contrast, is affected by vertical
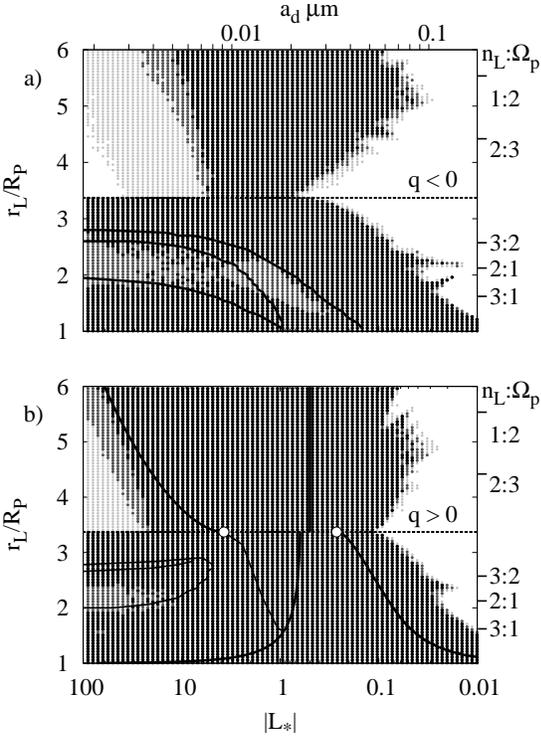
Fig. 17.— Stability of Kepler-launched grains in Neptune's full magnetic field, for twelve equally-spaced azimuthal launch positions, and integrated over one year. The greyscale is as in Fig. 16 with the darkest grey unstable for all launch longitudes and grains in the white areas surviving for all launch positions. As in previous figures, we superpose numerically-determined stability results for an aligned dipole as solid curves, and mark the local radial stability threshold at R_{syn}, where $L_* = 2 \pm \sqrt{3}$ with white circles.

impulses as might be expected, but also by azimuthal kicks which strengthen or weaken the magnetic mirror force. Finally, a radial kick barely affects dust grain motions at all.

When considering the stability of grains in the wide variety of planetary magnetic fields in the Solar System, we have shown in section 4 that dust grains with constant charges provide the maximum stability possible at each planet. The simplest magnetic field that we have considered, that of Saturn, is well-described as an untilted dipole, moderately offset to the north. This offset noticeably expands the vertical instability but has little discernable effect on radial motions.

Jupiter's magnetic field is substantially more complex than Saturn's with a moderate tilt, a southward offset, and sizeable higher-order field coefficients. The tilted dipole strongly affects vertical stability boundaries, and the loss of axisymmetry powers Lorentz Resonances. These resonances act to destabilize dust particles, allowing even negative grains outside synchronous orbit to escape from Jupiter. Thus the Io plasma torus, in which grains are expected to have negative charges, is not an impermeable barrier to escape. The high-speed dust streams detected by Ulysses and Galileo near Jupiter likely originate in the Io torus. We extend Lorentz resonances from the Kepler regime by rewriting their frequencies in terms of the general radial, vertical, and azimuthal frequencies valid at all charge-to-mass ratios. This allows us to calculate the radial locations of Lorentz resonances as a function of L_*. We note strong correlations between zones of instability and the predicted locations of Lorentz resonances. Finally, our numerical simulations show that some resonances with strengths proportional to L_*^2 must be active. We show how to determine the frequencies and rough stengths of these high-order resonances.

Our results for Jupiter are directly applicable to the Earth, which also has a magnetic field that is dominated by a moderately-tilted dipole. Two interesting differences, however, distinguish charged-particle motion at Earth from that at Jupiter. Firstly, due to its

inverted magnetic dipole, the radial instability at Earth affects negative not positive charges. Similarly, positively-charged dust at Earth behaves as negatively-charged dust at Jupiter. Secondly, the Earth is very small compared to the size of its synchronous orbital distance, minimizing the tendency of the vertical instability to force grains to collide with Earth. Furthermore, due to the rapid decay with distance of higher-order magnetic field terms, the effect of Earth's full magnetic field on dust grain trajectories differs little from that of a simple tilted dipole.

Uranus and Neptune both have complex magnetic field configurations which render aligned or even simple tilted dipolar models insufficient. Both of these planets have substantial quadrupolar and octupolar components, which act to destabilize both negative and positive grains across the synchronous orbital distance, and over a far greater range of charge-to-mass ratios than at the other planets that we have studied. These distant planets highlight how increases in magnetic field complexity dramatically exacerbate dynamical instabilities. Future spacecraft missions will provide more detailed planetary magnetic field configurations than we have available today, but changes to the stability maps that we have provided here for constant-charge dust grains are likely to be modest.

Relaxing the assumption of constant charge-to-mass ratios also leads to a substantial increase in the range of dust-grain sizes that are destabilized. Results are highly model-dependent, and for simplicity we adopted a sparse plasma with constant spatial density and photoelectric charging. The time-variable charging currents on a dust grain due to passage through the planetary shadow significantly expand the range of grain sizes that are globally unstable, particularly inside synchronous orbit. Larger dust grains respond rapidly to changes in the charging environment and hence stability is determined by comparing the destabilizing timescale of variable Lorentz forces with the orbital precession time (Horányi and Burns 1991; Hamilton and Krüger 2008). For our nominal model, this

increases the threshold radius for destabilized grains by more than an order of magnitude. For smaller grains, by contrast, charging is slow with the result that different stability curves apply at different times, expanding the zone of instability by an order of magnitude over that expected for a constant charge. The sparse plasma that we have adopted here is appropriate for the dusty main ring and gossamer rings at Jupiter. We find that the removal of dust at Jupiter is dominated by the basic dipolar radial instability for positive grains, substantially extended to both larger and smaller particles by the effects of variable charging. We leave a full study of the dependence of these effects on plasma parameters for a future study.

7. Acknowledgements

REFERENCES

Acuna, M. H., and N. F. Ness 1976. The main magnetic field of Jupiter. *J. Geophys. Res.* **81**, 2917–2922.

Bagenal, F. 1994. Empirical model of the Io plasma torus: Voyager measurements. *J. Geophys. Res.* **991**, 11043–11062.

Brooks, S. M., L. W. Esposito, M. R. Showalter, and H. B. Throop 2004. The size distribution of Jupiter's main ring from Galileo imaging and spectroscopy. *Icarus* **170**, 35–57.

Burns, J. A., L. E. Schaffer, R. J. Greenberg, and M. R. Showalter 1985. Lorentz resonances and the structure of the Jovian ring. *Nature* **316**, 115–119.

Burns, J. A., M. R. Showalter, D. P. Hamilton, P. D. Nicholson, I. de Pater, M. E. Ockert-Bell, and P. C. Thomas 1999. The Formation of Jupiter's Faint Rings. *Science* **284**, 1146–1150.

Cao, H., C. T. Russell, U. R. Christensen, M. K. Dougherty, and M. E. Burton 2011. Saturn's very axisymmetric magnetic field: No detectable secular variation or tilt. *Earth and Planetary Science Letters* **304**, 22–28.

Connerney, J. E. P., M. H. Acuna, and N. F. Ness 1991. The magnetic field of Neptune. *J. Geophys. Res.* **96**, 19023–19042.

Connerney, J. E. P., L. Davis, Jr., and D. L. Chenette 1984. *Magnetic field models*, pp. 354–377. University of Arizona Press.

Danby, J. M. A. 1988. Fundamentals of celestial mechanics. In Danby, J. M. A. (Ed.), *Richmond, Va., U.S.A. : Willmann-Bell, 1988. 2nd ed., rev. amp enl.*

de Pater, I., and J. Lissauer 2010. *Planetary Sciences*. Cambridge University Press.

de Pater, I., M. R. Showalter, J. A. Burns, P. D. Nicholson, M. C. Liu, D. P. Hamilton, and J. R. Graham 1999. Keck Infrared Observations of Jupiter's Ring System near Earth's 1997 Ring Plane Crossing. *Icarus* **138**, 214–223.

Dessler, A. J. 1983. *Physics of the Jovian magnetosphere*. Cambridge University Press.

Graps, A. L., E. Grün, H. Svedhem, H. Krüger, M. Horányi, A. Heck, and S. Lammers 2000. Io as a source of the jovian dust streams. *Nature* **405**, 48–50.

Hamilton, D. P. 1993a. Motion of dust in a planetary magnetosphere - Orbit-averaged equations for oblateness, electromagnetic, and radiation forces with application to Saturn's E ring. *Icarus* **101**, 244–264.

Hamilton, D. P. 1993b. Erratum: "motion of Dust in a Planetary Magnetosphere: Orbit-Averaged Equations for Oblateness, Electromagnetic, and Radiation Forces with Application to Saturn's E-Ring. *Icarus* **103**, 161.

Hamilton, D. P. 1994. A comparison of Lorentz, planetary gravitational, and satellite gravitational resonances. *Icarus* **109**, 221–240.

Hamilton, D. P. 1996. Dust from Jupiter's Gossamer Ring and the Galilean Satellites. In *Bulletin of the American Astronomical Society*, Volume 28 of *Bulletin of the American Astronomical Society*, pp. 1123.

Hamilton, D. P., and J. A. Burns 1993a. Ejection of dust from Jupiter's gossamer ring. *Nature* **364**, 695–699.

Hamilton, D. P., and J. A. Burns 1993b. Lorentz and gravitational resonances on circumplanetary particles. *Advances in Space Research* **13**, 241–248.

Hamilton, D. P., and H. Krüger 2008. The sculpting of Jupiter's gossamer rings by its shadow. *Nature* **453**, 72–75.

Hedman, M. M., J. A. Burns, M. R. Showalter, C. C. Porco, P. D. Nicholson, A. S. Bosh, M. S. Tiscareno, R. H. Brown, B. J. Buratti, K. H. Baines, and R. Clark 2007. Saturn's dynamic D ring. *Icarus* **188**, 89–107.

Horányi, M., and J. A. Burns 1991. Charged dust dynamics - Orbital resonance due to planetary shadows. *J. Geophys. Res.* **96**, 19283–19289.

Horányi, M., J. A. Burns, and D. P. Hamilton 1992. The dynamics of Saturn's E ring particles. *Icarus* **97**, 248–259.

Horányi, M., H. L. F. Houpis, and D. A. Mendis 1988. Charged dust in the earth's magnetosphere. I - Physical and dynamical processes. *Ap&SS* **144**, 215–229.

Horányi, M., and A. Juhász 2010. Plasma conditions and the structure of the Jovian ring. *Journal of Geophysical Research (Space Physics)* **115**, A09202 1–12.

Horányi, M., G. Morfill, and E. Grün 1993a. Mechanism for the acceleration and ejection of dust grains from Jupiter's magnetosphere. *Nature* **363**, 144–146.

Horányi, M., G. Morfill, and E. Grün 1993b. The dusty ballerina skirt of Jupiter. *J. Geophys. Res.* **98**, 21245–21251.

Jontof-Hutter, D., and D. P. Hamilton 2012. The Fate of Sub-Micron Circumplanetary Dust Grains I: Aligned Dipolar Magnetic Fields. *Icarus* **218**, 420–432.

Juhász, A., and M. Horányi 1997. Dynamics of charged space debris in the Earth's plasma environment. *J. Geophys. Res.* **102**, 7237–7246.

Krüger, H., P. Geissler, M. Horányi, A. L. Graps, S. Kempf, R. Srama, G. Moragas-Klostermeyer, R. Moissl, T. V. Johnson, and E. Grün 2003. Jovian dust streams: A monitor of Io's volcanic plume activity. *Geophys. Res. Lett. 30*(21), 2101.

Krüger, H., D. P. Hamilton, R. Moissl, and E. Grün 2009. Galileo in-situ dust measurements in Jupiter's gossamer rings. *Icarus* **203**, 198–213.

Mendis, D. A., H. L. F. Houpis, and J. R. Hill 1982. The gravito-electrodynamics of charged dust in planetary magnetospheres. *J. Geophys. Res.* **87**, 3449–3455.

Mitchell, C. J., M. Horányi, and J. E. Howard 2003. Accuracy of epicyclic description of dust grain orbits about Saturn. *Journal of Geophysical Research (Space Physics)* **108**.

Ness, N. F., J. E. P. Connerney, R. P. Lepping, M. Schulz, and G.-H. Voigt 1991. The magnetic field and magnetospheric configuration of Uranus. In J. T. Bergstralh, E. D. Miner, and M. S. Matthews (Eds.), *Uranus*, pp. 739–779. University of Arizona Press.

Northrop, T. G., and J. E. P. Connerney 1987. A micrometeorite erosion model and the age of Saturn's rings. *Icarus* **70**, 124–137.

Northrop, T. G., and J. R. Hill 1982. Stability of negatively charged dust grains in Saturn's ring plane. *J. Geophys. Res.* **87**, 6045–6051.

Northrop, T. G., and J. R. Hill 1983. The inner edge of Saturn's B ring. *J. Geophys. Res.* **88**, 6102–6108.

Ockert-Bell, M. E., J. A. Burns, I. J. Daubar, P. C. Thomas, J. Veverka, M. J. S. Belton, and K. P. Klaasen 1999. The Structure of Jupiter's Ring System as Revealed by the Galileo Imaging Experiment. *Icarus* **138**, 188–213.

Owen, T., G. E. Danielson, A. F. Cook, C. Hansen, V. L. Hall, and T. C. Duxbury 1979. Jupiter's rings. *Nature* **281**, 442–446.

Roberts, P. H., and A. M. Soward 1972. Magnetohydrodynamics of the Earth's Core. *Annual Review of Fluid Mechanics* **4**, 117–154.

Schaffer, L., and J. A. Burns 1987. The dynamics of weakly charged dust - Motion through Jupiter's gravitational and magnetic fields. *J. Geophys. Res.* **92**, 2264–2280.

Schaffer, L., and J. A. Burns 1992. Lorentz resonances and the vertical structure of dusty rings - Analytical and numerical results. *Icarus* **96**, 65–84.

Schaffer, L., and J. A. Burns 1994. Charged dust in planetary magnetospheres: Hamiltonian dynamics and numerical simulations for highly charged grains. *J. Geophys. Res.* **99**, 17211–17223.

Showalter, M. R. 1996. Saturn's D Ring in the Voyager Images. *Icarus* **124**, 677–689.

Showalter, M. R., I. de Pater, G. Verbanac, D. P. Hamilton, and J. A. Burns 2008. Properties and dynamics of Jupiter's gossamer rings from Galileo, Voyager, Hubble and Keck images. *Icarus* **195**, 361–377.

Throop, H. B., C. C. Porco, R. A. West, J. A. Burns, M. R. Showalter, and P. D. Nicholson 2004. The jovian rings: new results derived from Cassini, Galileo, Voyager, and Earth-based observations. *Icarus* **172**, 59–77.

Valk, S., and A. Lemaître 2008. Semi-analytical investigations of high area-to-mass ratio geosynchronous space debris including Earth's shadowing effects. *Advances in Space Research* **42**, 1429–1443.